

Adaptive variational quantum computing approaches for Green’s functions and nonlinear susceptibilities

Martin Mootz,^{1,*} Thomas Iadecola,^{1,2} and Yong-Xin Yao^{1,2,†}

¹*Ames National Laboratory, U.S. Department of Energy, Ames, Iowa 50011, USA*

²*Department of Physics and Astronomy, Iowa State University, Ames, Iowa 50011, USA*

We present and benchmark quantum computing approaches for calculating real-time single-particle Green’s functions and nonlinear susceptibilities of Hamiltonian systems. The approaches leverage adaptive variational quantum algorithms for state preparation and propagation. Using automatically generated compact circuits, the dynamical evolution is performed over sufficiently long times to achieve adequate frequency resolution of the response functions. We showcase accurate Green’s function calculations using a statevector simulator for Fermi-Hubbard chains of 4 and 6 sites, with maximal circuit depth of 65 and 424 layers, respectively. Additionally, we consider an antiferromagnetic quantum spin-1 model that incorporates the Dzyaloshinskii-Moriya interaction to illustrate calculations of the third-order nonlinear susceptibilities, which can be measured in two-dimensional coherent spectroscopy experiments. These results demonstrate that real-time approaches using adaptive parameterized circuits to evaluate linear and nonlinear response functions can be feasible with near-term quantum processors.

I. INTRODUCTION

In the pursuit of understanding and predicting the properties of quantum systems, the development of efficient computational methodologies has become imperative. Among the plethora of tools available, the calculation of Green’s functions [1, 2] and related high-order nonlinear susceptibilities [3–5] provide crucial insights into dynamical responses, correlation effects, and excitations within complex quantum systems. Specifically, many-particle Green’s functions describe the correlations and interactions among particles in quantum systems via correlation functions or response functions and also facilitate the development of advanced theoretical frameworks for describing complex quantum phenomena such as the GW method [6] and dynamical mean-field theory [7–9]. These methods rely heavily on Green’s functions to investigate the rich phenomena exhibited by complex materials, including superconductivity [10], magnetism [11], and topological phases [12]. Central to the analysis of Green’s functions is the concept of spectral functions, which provide a direct link between theoretical calculations and measurable quantities in experiments, such as photoemission spectra [13], optical conductivity [14], or neutron scattering cross-sections [15]. In contrast, nonlinear susceptibilities [3–5] offer a systematic approach to analyze the nonlinear optical response of quantum systems to multiple interacting laser pulses. Specifically, two-dimensional coherent spectroscopy (2DCS) [16–31] directly probes nonlinear susceptibilities by measuring the time-dependent coherent response to two laser pulses.

Traditional methods for computing Green’s functions and nonlinear susceptibilities, such as exact diagonalization (ED) [32], density-matrix renormalization group [33],

or quantum Monte Carlo simulation [34], often face challenges in simulating large-scale systems at low temperatures. Nevertheless, in recent years the advent of quantum computing [35] has opened up new avenues for tackling these challenges. These simulations hold promise in providing valuable insights into the properties of complex quantum materials that go beyond what is possible with classical computers [36]. So far, these simulations have been conducted on noisy intermediate-scale quantum (NISQ) devices [37–41], which are restricted by the available number of qubits and by hardware noise. Several methods have been proposed to calculate Green’s functions and multi-time correlation functions [42] in frequency space using quantum-phase estimation [43–46], and in the time domain using the Suzuki-Trotter decomposition of the time evolution operator [47–49]. However, these techniques demand deep quantum circuits and large numbers of controlled operations, making them impractical for NISQ hardware. To address these issues, several quantum circuit compression algorithms have been introduced. These algorithms calculate Green’s functions in the frequency domain using the variational quantum eigensolver (VQE) [50, 51], or in the time domain by simplifying the time evolution unitary operation using the coupled cluster Green’s function method [52], Cartan decomposition [53], or variational quantum dynamics simulation (VQDS) algorithms [50, 54, 55]. The latter involves the preparation of a variational ansatz state to approximate the exact time-evolved state of the system. The equation of motion governing the time evolution of the variational parameters is derived based on the McLachlan variational principle [54, 56, 57], which aims to minimize the distance between the variational state and the exact time-evolved state.

Nonetheless, the efficacy of VQDS crucially depends on the flexibility of the variational ansatz to faithfully represent the dynamical states of the system. Using Hamiltonian variational ansatz (HVA) [50, 55], the accuracy of the real-time Green’s function can be improved

* mootz@iastate.edu

† ykent@iastate.edu

by increasing the number of layers, i.e., the depth of the ansatz. However, a large number of layers can be required to precisely describe the quantum state dynamics over sufficiently long times to achieve adequate resolution of correlation function in frequency space, leading to large circuit depths. Adaptive variational algorithms, such as the adaptive variational quantum dynamics simulation (AVQDS) [58] approach, can automatically generate problem-specific ansätze with reduced complexity compared to general problem-agnostic fixed ansatz [58–60]. In AVQDS, the McLachlan distance, a metric to measure the difference between the variational and exact state evolutions, is maintained below a predefined threshold throughout the time evolution by adaptively adding new parameterized unitaries chosen from a predetermined operator pool to the variational ansatz. This method has been applied in Ref. [61] to calculate the single-particle Green’s function using a Hadamard-test circuit to compute state overlaps. The result in Ref. [61] demonstrates that less quantum resources are required compared to VQDS with HVA, even as the accuracy over long simulation times is improved. However, the Hadamard-test circuit involves controlled multi-qubit rotation gates for state propagation, which can substantially increase the circuit complexity.

In this work, we employ the AVQDS algorithm to calculate single-particle Green’s functions and nonlinear susceptibilities along the real-time axis. In contrast to the controlled-unitaries-required (CUR) approach for overlap testing [61], we adopt the method presented in Ref. [50], which is controlled-unitaries-liberated (CUL) and applies to generic reference states besides the ground state. Instead, the method requires the parametrized circuit to directly simulate the dynamics of two quantum states, as opposed to one in the CUR method [55, 61]. The CUL calculation is conveniently performed on circuits with an ancilla qubit plus a few controlled Pauli gates to mix the two quantum states, followed by state evolution. Although the simultaneous propagation of two states instead of one demands more flexible circuits, it allows one to leverage the variational degrees of freedom already existing in the initial parameterized state (e.g., the ground state) for variational state propagation using more compact circuits. We apply the CUL approach to calculate the single-particle Green’s functions of Fermionic models using the AVQDS approach instead of VQDS with HVA as in Ref. [50]. Additionally, we extend this method to calculate nonlinear susceptibilities of quantum spin models, which depend on two times and thus requires double application of the AVQDS approach to evolve the quantum states.

To illustrate the calculation of Green’s functions with the AVQDS approach, we study the single-particle Green’s functions of Fermi-Hubbard chains with $N = 4$ and $N = 6$ sites, corresponding respectively to 8 and 12 qubits. Using statevector simulations, we calculate the Green’s function dynamics in momentum space and discuss the required quantum resources for near-term applications measured

by number of CNOT gates and circuit layers. Additionally, by applying the Padé approximation, we compute the spectral function and compare the results obtained with the circuit simulator to exact results derived from the Lehmann representation of the Green’s function. To demonstrate the validity of our method to calculate high-order susceptibilities measured in two-dimensional coherent spectroscopy experiments, we consider an antiferromagnetic quantum high-spin model that incorporates the Heisenberg exchange and Dzyaloshinskii-Moriya interaction [62]. Specifically, we calculate the third-order nonlinear susceptibility in the two-dimensional (2D) time and frequency domain for a two-site spin-1 model and compare with exact numerical results.

The paper is organized as follows. The AVQDS algorithm is briefly discussed in Sec. II. In Sec. III we present the algorithm for calculating single-particle Green’s functions. In Sec. IV we calculate the Green’s function and corresponding spectral functions for $N = 4$ and $N = 6$ Fermi-Hubbard chains and benchmark the performance of the AVQDS approach. The method for simulating nonlinear susceptibilities is presented in Sec. V. In Sec. VI, we demonstrate the algorithm by calculating the third-order susceptibility of a two-site spin-1 model. Finally, we conclude in Sec. VII with a summary of findings and an outlook.

II. AVQDS ALGORITHM

In this work, we employ the AVQDS algorithm as a quantum computing approach to calculate Green’s functions and high-order nonlinear susceptibilities. Below, we briefly discuss the key points of AVQDS, while a more detailed discussion can be found in Refs. [58, 62]. The algorithm can be naturally extended from real-time dynamics to the adaptive variational quantum imaginary-time evolution (AVQITE) approach [59], which is adopted for ground state preparation in the following calculations. We begin by considering a quantum system initially in the pure state $|\Psi\rangle$, whose quantum dynamics is governed by a generally time-dependent Hamiltonian $\hat{\mathcal{H}}$. The dynamics of the system’s density matrix $\rho = |\Psi\rangle\langle\Psi|$ is then determined by the von Neumann equation:

$$\frac{d\rho}{dt} = -i \left[\hat{\mathcal{H}}, \rho \right]. \quad (1)$$

In variational quantum dynamics simulations, the state $|\Psi\rangle$ is parameterized as $|\Psi[\boldsymbol{\theta}]\rangle$, with $\boldsymbol{\theta}(t)$ being a real-valued time-dependent variational parameter vector of dimension N_θ [54]. The evolution of $\boldsymbol{\theta}$ is determined by equations of motion derived from the McLachlan variational principle [63], which minimizes the squared McLachlan distance \mathcal{L}^2 as the Frobenius norm ($\|\mathcal{O}\| \equiv \text{Tr}[\mathcal{O}^\dagger \mathcal{O}]$)

between exact and variational evolving states:

$$\begin{aligned} \mathcal{L}^2 &\equiv \left\| \sum_{\mu} \frac{\partial \rho[\theta]}{\partial \theta_{\mu}} \dot{\theta}_{\mu} + i [\hat{\mathcal{H}}, \rho] \right\|^2 \\ &= \sum_{\mu\nu} M_{\mu\nu} \dot{\theta}_{\mu} \dot{\theta}_{\nu} - 2 \sum_{\mu} V_{\mu} \dot{\theta}_{\mu} + 2 \text{var}_{\theta}[\hat{\mathcal{H}}], \end{aligned} \quad (2)$$

where the $N_{\theta} \times N_{\theta}$ matrix M and vector V of dimension N_{θ} are defined as

$$\begin{aligned} M_{\mu,\nu} &\equiv \text{Tr} \left[\frac{\partial \rho[\theta]}{\partial \theta_{\mu}} \frac{\partial \rho[\theta]}{\partial \theta_{\nu}} \right] = 2 \text{Re} \left[\frac{\partial \langle \Psi[\theta] |}{\partial \theta_{\mu}} \frac{\partial |\Psi[\theta]\rangle}{\partial \theta_{\nu}} \right. \\ &\quad \left. + \frac{\partial \langle \Psi[\theta] |}{\partial \theta_{\mu}} |\Psi[\theta]\rangle \frac{\partial \langle \Psi[\theta] |}{\partial \theta_{\nu}} |\Psi[\theta]\rangle \right], \end{aligned} \quad (3)$$

$$V_{\mu} = 2 \text{Im} \left[\frac{\partial \langle \Psi[\theta] |}{\partial \theta_{\mu}} \hat{\mathcal{H}} |\Psi[\theta]\rangle + \langle \Psi[\theta] | \frac{\partial |\Psi[\theta]\rangle}{\partial \theta_{\mu}} \langle \hat{\mathcal{H}} \rangle_{\theta} \right], \quad (4)$$

with $\langle \hat{\mathcal{H}} \rangle_{\theta} = \langle \Psi[\theta] | \hat{\mathcal{H}} | \Psi[\theta] \rangle$. The real symmetric matrix M is directly related to the quantum Fisher information matrix [64], with the second term within the bracket accounting for the global phase contribution [54]. In the last term of Eq. (2), $\text{var}_{\theta}[\hat{\mathcal{H}}] = \langle \hat{\mathcal{H}}^2 \rangle_{\theta} - \langle \hat{\mathcal{H}} \rangle_{\theta}^2$ is the variance of $\hat{\mathcal{H}}$ in the variational state $|\Psi[\theta]\rangle$. The minimization of \mathcal{L}^2 with respect to $\{\dot{\theta}_{\mu}\}$ leads to the equation:

$$\sum_{\nu} M_{\mu\nu} \dot{\theta}_{\nu} = V_{\mu}, \quad (5)$$

which governs the dynamics of the variational parameters. The optimized McLachlan distance for the variational ansatz $|\Psi[\theta]\rangle$,

$$L^2 = 2 \text{var}_{\theta}[\hat{\mathcal{H}}] - \sum_{\mu} V_{\mu} \dot{\theta}_{\mu}, \quad (6)$$

is a metric quantifying the accuracy of the variational dynamics.

In the AVQDS framework, the ansatz takes a pseudo-Trotter form:

$$|\Psi[\theta]\rangle = \prod_{\mu=1}^{N_{\theta}} e^{-i\theta_{\mu} \hat{\mathcal{A}}_{\mu}} |\varphi_0\rangle. \quad (7)$$

Here, $\hat{\mathcal{A}}_{\mu}$ ($\mu = 1, \dots, N_{\theta}$) represent Hermitian generators, while $|\varphi_0\rangle$ denotes the reference state. To maintain the McLachlan distance L^2 below a given threshold L_{cut}^2 throughout the time evolution, operators are dynamically selected from a predefined pool of generators, which expands the set of unitaries in the ansatz (7). The selection criterion is to add to the ansatz the operator that maximally reduces L^2 , so as to achieve accurate dynamics simulations with the minimal number of unitaries. In the initial proposal of the AVQDS approach [58], operators were chosen one by one; here we adopt a modified strategy. Specifically, multiple operators, rather than a

single one, are simultaneously chosen according to the L^2 -criterion at each iteration, subject to the constraint that these operators act on disjoint sets of qubits. This approach takes the spatial compactness of the circuits into account, and significantly reduces the circuits depth with only a small change in the total number of CNOT gates. The ansatz expansion is done by first calculating the McLachlan distance L_{ν}^2 for a new variational ansatz of the form $e^{-i\theta_{\nu} \hat{\mathcal{A}}_{\nu}} |\Psi[\theta]\rangle$ for all generators $\hat{\mathcal{A}}_{\nu}$ from a predefined operator pool of size N_p . The resulting L_{ν}^2 are ordered in ascending order. In the first step, the operator $\hat{\mathcal{A}}_{\nu}$ leading to the smallest L_{ν}^2 is added to the ansatz (7), which increases $N_{\theta} \rightarrow N_{\theta} + 1$ in Eq. (7). In the next step, the operator with the next smallest L_{ν}^2 is appended, provided it acts on different qubits than the first operator. This process continues by adding operators with successively larger or equal L_{ν}^2 that have disjoint supports from all previously appended operators during this iteration, until all qubits are covered or no more suitable operators are found. Note that this method does not introduce additional L_{ν}^2 measurements, as L^2 for each pool operator is measured once per iteration. The variational parameters θ_{ν} are set to zero for all operators appended to the ansatz (7) during the iteration step. This does not alter the ansatz state but can modify the McLachlan distance L^2 due to a non-zero derivative with respect to θ_{ν} . Finally, L^2 is calculated for the new ansatz and compared with L_{cut}^2 . This adaptive procedure is repeated until the McLachlan distance L^2 of the new ansatz falls below L_{cut}^2 .

In the simulations performed in this work, we solve Eq. (5) using a fourth-order Runge-Kutta method. While this method involves computational overhead due to each time step requiring four micro-time steps to update the variational parameters (compared to Euler's method, which updates parameters in a single step) it still substantially reduces the total number of time steps and circuit complexity, as demonstrated in Ref. [62]. Additionally, the time step δt in the AVQDS approach is dynamically adjusted to ensure that $\max_{0 \leq \mu < N_{\theta}} |\delta \theta_{\mu}|$ remains below a predefined maximal step size $\delta \theta_{\text{max}}$, where $\delta \theta_{\mu} = \theta_{\mu}(t + \delta t) - \theta_{\mu}(t)$. In the simulations we set $\delta \theta_{\text{max}} = 0.01$. Furthermore, to mitigate potential numerical issues associated with inverting the matrix M in Eq. (5), we employ the Tikhonov regularization approach, where a small number of $\delta = 10^{-6}$ is added to the diagonal of M . This stabilizes the matrix inversion process, especially when M possesses a high condition number.

To benchmark the performance of AVQDS, we compare the AVQDS results with results utilizing exact diagonalization for state propagation:

$$|\Psi[t + \delta t]\rangle = e^{-i\delta t \hat{\mathcal{H}}[t]} |\Psi[t]\rangle. \quad (8)$$

This simulation is performed on a uniformly discretized time grid with a step size of $\delta t = 0.002$. Since our study focuses on time-independent Hamiltonians, the error due to finite time mesh here is zero.

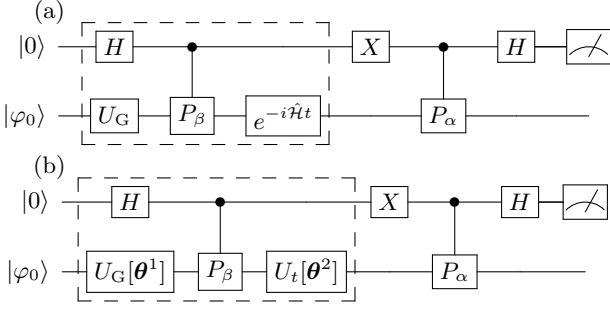


FIG. 1. **Hadamard test circuit to compute the Green's function.** (a) Circuit to measure the Green's function component $I_{\alpha,\beta}^{p,q}$ (12) using the exact time-evolution operator $e^{-i\hat{H}t}$. The ancillary qubit, initially in the state $|0\rangle$, is represented by the upper horizontal line. X and H denote Pauli- X and Hadamard gates on the ancilla, respectively. A register of qubits for the physical system of interest, initially in a reference product state $|\varphi_0\rangle$, is denoted by the lower horizontal line. The application of the general multi-qubit Pauli gates P_α and P_β is controlled by the ancilla qubit, while the unitary operator U_G prepares the ground state, $|G\rangle = U_G |\varphi_0\rangle$. (b) Measurement circuit for $I_{\alpha,\beta}^{p,q}$ using a variational state evolution circuit. The state propagation circuit highlighted with the dashed rectangle in (a) is replaced by the (adaptive) variational circuit in (b), where the angles in the parameterized unitaries $U_G[\theta^1]$ and $U_t[\theta^2]$ evolve with time. The results are obtained from Z -basis measurements on the ancilla qubit.

III. COMPUTATION OF GREEN'S FUNCTIONS WITH AVQDS

We begin by considering a time-independent fermionic Hamiltonian $\hat{\mathcal{H}}$, expressed in terms of fermionic operators \hat{c}_p^\dagger and \hat{c}_p that create and annihilate an electron in orbital site $p = (j, \sigma)$. Here j is the site index and σ corresponds to the spin of the fermion. The dynamics of the system at zero temperature is described by the retarded single-particle Green's function:

$$G_{p,q}^R(t) = -i\Theta(t) \left[\langle G | \hat{c}_p(t) \hat{c}_q^\dagger(0) | G \rangle + \langle G | \hat{c}_q^\dagger(0) \hat{c}_p(t) | G \rangle \right]. \quad (9)$$

Here, $\hat{c}_p(t) = e^{i\hat{H}t} \hat{c}_p e^{-i\hat{H}t}$ corresponds to the Heisenberg representation of the fermionic operator \hat{c}_p , $\Theta(t)$ is the Heaviside step function, and $|G\rangle$ denotes the ground state of Hamiltonian $\hat{\mathcal{H}}$.

To calculate Eq. (9) using a quantum computer, we adopt the Jordan-Wigner transformation [65] to map the fermionic operators to Pauli operators as:

$$\hat{c}_p = \sum_\alpha \eta_\alpha^{(p)} P_\alpha^{(p)}. \quad (10)$$

Here, $\eta_\alpha^{(p)}$ are complex-valued numbers and $P_\alpha^{(p)}$ are Pauli words up to a weight of N_q , which is the number of qubits required to encode the Fermionic Hamiltonian $\hat{\mathcal{H}}$. Using

transformation (10), Eq. (9) can be rewritten as:

$$G_{p,q}^R(t) = -i\Theta(t) \sum_{\alpha,\beta} \eta_\alpha^{(p)} \eta_\beta^{(q)} \left[\langle G | e^{i\hat{H}t} P_\alpha^{(p)} e^{-i\hat{H}t} P_\beta^{(q)} | G \rangle + \langle G | P_\beta^{(q)} e^{i\hat{H}t} P_\alpha^{(p)} e^{-i\hat{H}t} | G \rangle \right] \equiv -2i\Theta(t) \sum_{\alpha,\beta} \eta_\alpha^{(p)} \eta_\beta^{(q)} I_{\alpha,\beta}^{p,q}, \quad (11)$$

with

$$I_{\alpha,\beta}^{p,q} \equiv \text{Re} \left[\langle G | e^{i\hat{H}t} P_\alpha^{(p)} e^{-i\hat{H}t} P_\beta^{(q)} | G \rangle \right]. \quad (12)$$

Equation (12) can be measured using a Hadamard test circuit on a quantum computer, as shown in Fig. 1 (a). The time evolution operator $e^{-i\hat{H}t}$ can be approximated using Trotter decomposition [66–68] or VQDS algorithms [54], including AVQDS [58].

In this work, we first use the AVQITE algorithm to prepare the ground state of a Hamiltonian system, $|G[\theta^1]\rangle = U_G[\theta^1] |\varphi_0\rangle$, with a series of parameterized unitaries $U_G[\theta^1]$ applied to a reference product state $|\varphi_0\rangle$. The time propagation of the ancilla and physical register, as outlined by the dashed box in Fig. 1 (a), is achieved by a parameterized circuit highlighted by the dashed box in Fig. 1 (b). The additional unitaries $U_t[\theta^2]$ are automatically generated following the AVQDS algorithm. The rotation angles θ^1 and θ^2 both evolve according to the equation of motion (5). In other words, AVQDS is adopted for the time propagation of the state

$$|\Psi\rangle = \frac{1}{\sqrt{2}} |0\rangle \otimes |G\rangle + \frac{1}{\sqrt{2}} |1\rangle \otimes P_\beta |G\rangle \quad (13)$$

under a Hamiltonian that acts only on the physical register. As shown in Appendix A, the circuit in Fig. 1 (b) measures the Green's function component as

$$I_{\alpha,\beta}^{p,q} \approx \text{Re} \left[\langle G[\theta^1] | U_t^\dagger[\theta^2] P_\alpha^{(p)} U_t[\theta^2] P_\beta^{(q)} | G[\theta^1] \rangle \right]. \quad (14)$$

IV. SINGLE-PARTICLE GREEN'S FUNCTION OF FERMI-HUBBARD CHAINS

A. Model

To benchmark the performance of the AVQDS approach in calculating the Green's function as outlined in Sec. III and to compare the results with alternative approaches in Refs. [50, 55, 61], we study the one-dimensional Fermi-Hubbard model of N sites in its particle-hole-symmetric form:

$$\hat{\mathcal{H}} = -t \sum_{\langle i,j \rangle, \sigma} \left(\hat{c}_{i,\sigma}^\dagger \hat{c}_{j,\sigma} + \text{h.c.} \right) + U \sum_j n_{j,\uparrow} n_{j,\downarrow} - \frac{U}{2} \sum_{j,\sigma} n_{j,\sigma}. \quad (15)$$

Here, $\hat{c}_{j,\sigma}$ denotes the annihilation operator for a fermion with spin σ at site j , $n_{j,\sigma}$ represents the number operator, t denotes the hopping amplitude between neighboring sites, and U corresponds to the on-site interaction strength. We focus on $N = 4$ and $N = 6$ -site chains with open boundary conditions. Specifically, we set the hopping parameter $t = 1$ and the on-site interaction is fixed at $U = 4.0$. To map Hamiltonian (15) to multi-qubit operators, we utilize the Jordan-Wigner transformation [65]. The encoding of Hamiltonian (15) requires $N_q = 8$ and $N_q = 12$ qubits for $N = 4$ and $N = 6$ -site systems, respectively.

B. Ground state preparation

The ground state is prepared using the AVQITE approach [59], where the distance between the actual imaginary time-evolved state and the variational ansatz state is minimized in accordance with McLachlan's variational principle [63]. Analogous to AVQDS, the McLachlan distance is kept below a predefined threshold during the imaginary time evolution by adaptively appending new parameterized unitaries to the variational ansatz. The generators of the unitaries are chosen from a predetermined operator pool. The obtained ground state ansatz also takes the pseudo-Trotter form (7), allowing straightforward combination with the AVQDS approach.

In our simulations, we adopt an operator pool derived from the unitary coupled-cluster singles and doubles (UCCSD) excitation operators [69, 70], or the related qubit excitation operators [71]. Specifically, the pool can be written as:

$$\mathcal{P} = \{\hat{\sigma}_i^p \hat{\sigma}_j^q\} \cup \{\hat{\sigma}_i^p \hat{\sigma}_j^q \hat{\sigma}_k^r \hat{\sigma}_l^s\}, \quad (16)$$

subject to the constraint that only Pauli strings with odd number of $\hat{\sigma}^y$ are included. Here $p, q, r, s \in \{x, y\}$, i, j, k, l run over all qubits, and $\hat{\sigma}^x$ and $\hat{\sigma}^y$ represent Pauli operators. The pool comprises $N_p = 616$ generators for the model with $N = 4$ and $N_p = 4092$ generators for $N = 6$. Regarding the reference state $|\varphi_0\rangle$, we opt for a product state with spin-up electrons occupying fermionic orbital sites $1, \dots, N/2$ and spin-down electrons for sites $N/2 + 1, \dots, N$, which is subsequently converted to a product state in the qubit representation. Although there are many other forms of reference states [72], such as a product state from Hartree-Fock or qubit mean-field calculations [73], this choice is consistent with Ref. [61], which allows a fair comparison on quantum resources between the CUR [61] and our CUL approaches.

C. Simulation results

We first analyze the performance and quantum resource requirements for the algorithm outlined in Sec. III. For the operator pool in the AVQDS calculations, we utilize

the Hamiltonian operator pool, which encompasses all individual Pauli strings contained in the qubit representation of the Hamiltonian. As a result, the pool comprises $N_p = 16$ ($N_p = 26$) operators for $N = 4$ ($N = 6$) model. To compute the Green's function $G_{p,q}^R(t)$ using Eq. (11), the quantum circuit in Fig. 1 (b) needs to be calculated for all α, β -components in Eq. (11). Since the expression of the creation or annihilation operators according to Eq. (10) consists of $n = 2$ terms after the Jordan-Wigner transformation, computing the Green's function via Eq. (11) involves $n^2 = 4$ simulations of the quantum circuit in Fig. 1 (b) for a given p, q -component.

Figures 2 (a) and 2 (b) show examples of the $I_{\alpha,\beta}^{p,q}$ dynamics for different combinations of p, q, α , and β , obtained by evaluating the quantum circuit presented in Fig. 1 (b) for the $N = 4$ - and $N = 6$ -site Fermi-Hubbard chains. The results of the AVQDS approach (solid lines) are plotted together with the corresponding outcomes of the exact simulation (black dashed lines) obtained via exact diagonalization (8). The AVQDS results closely align with those of the exact simulations for all presented $I_{\alpha,\beta}^{p,q}$. To quantify the precision of the AVQDS calculations, we plot the corresponding infidelity in Figs. 2 (c) and 2 (d), defined as $1 - f = 1 - |\langle \Psi[\theta(t)] | \Psi_{\text{exact}}(t) \rangle|^2$. Here, $|\Psi_{\text{exact}}[t]\rangle = I \otimes e^{-i\hat{H}t} |\Psi\rangle$ with $|\Psi\rangle$ defined in Eq. (13) is calculated using exact diagonalization (8), while $|\Psi[\theta(t)]\rangle$ represents the corresponding variational wavefunction obtained through AVQDS. The infidelity remains below 7.1×10^{-4} (3.6×10^{-3}) within the studied time window for the $N = 4$ -site ($N = 6$ -site) simulations. This demonstrates that on a statevector simulator AVQDS can accurately calculate the real-time Green's function components $I_{\alpha,\beta}^{p,q}$ using the quantum circuit presented in Fig. 1 (b).

The above results are obtained from noiseless statevector simulations and therefore neglect the effects of gate errors as well as finite sampling of the quantum state when measuring the matrix M and vector V in Eqs. (3) and (4). Thus, it is important to estimate the quantum resources necessary for AVQDS calculations on NISQ devices. Our focus here is on the quantum circuit complexity quantified by the number of two-qubit CNOT gates. To simplify the analysis, we assume full qubit connectivity, as found in trapped-ion architecture, where implementing the multi-qubit rotation gate $e^{-i\theta\hat{A}}$ demands $2(p-1)$ CNOT gates for a Pauli string \hat{A} containing p Pauli operators. Figures 2 (e) and 2 (f) show the growth of the CNOT number with time for the $I_{\alpha,\beta}^{p,q}$ simulations presented in Figs. 2 (a) and 2 (b). The AVQITE ground-state preparation achieves an infidelity of approximately 10^{-6} and 3.6×10^{-5} for $N = 4$ and $N = 6$, respectively. The number of variational parameters N_θ required for the ground state preparation is 65 for $N = 4$ and 551 for $N = 6$. Specifically, the associated variational ansatz (7) incorporates 30 two- and 35 four-qubit rotation gates for $N = 4$, resulting in 270 CNOTs, and 226 two- and 325 four-qubit rotation gates for $N = 6$, yielding 2402

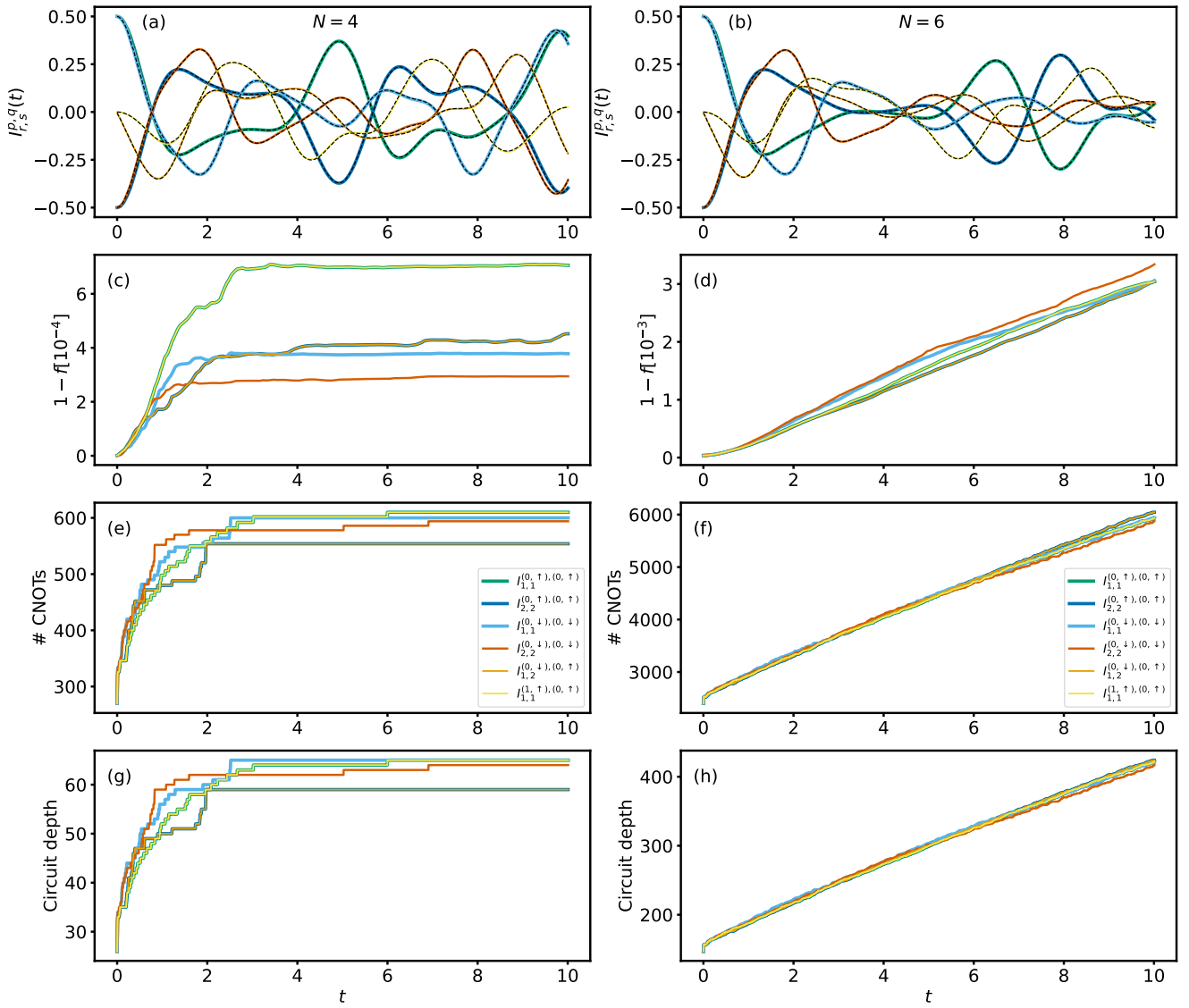


FIG. 2. Numerical simulation of the AVQDS approach for computing the single-particle Green's function of Fermi-Hubbard model. Examples of $I_{\alpha,\beta}^{p,q}(t)$ dynamics for six different combinations of p , q , α , and β , obtained by evaluating the quantum circuit in Fig. 1 (b) for Fermi-Hubbard chains with (a) $N = 4$ - and (b) $N = 6$ -sites. The results obtained with the AVQDS approach (solid lines) are compared with those of the exact simulations (black dashed lines) obtained via exact diagonalization (8). The corresponding infidelities $1 - f$ in (c) and (d) demonstrate the high accuracy of AVQDS in calculating the Green's function components $I_{\alpha,\beta}^{p,q}(t)$, achieving a fidelity of at least 99.93 % for $N = 4$ and 99.64 % for $N = 6$. The corresponding number of CNOT gates in (e) and (f) increases from an initial count of 270 (2402) to a maximum of 610 (6148) at the final simulation time of $t = 10$ for $N = 4$ ($N = 6$). The circuit depth in (g) and (h) grows from 26 (147) to a maximum circuit depth of 65 (424) at $t = 10$ for $N = 4$ ($N = 6$). Note that the pair $I_{1,1}^{(0,\uparrow),(0,\uparrow)}$ (green line) and $I_{1,1}^{(1,\uparrow),(0,\uparrow)}$ (yellow line) as well as the pair $I_{2,2}^{(0,\uparrow),(0,\uparrow)}$ (dark blue line) and $I_{1,2}^{(0,\downarrow),(0,\uparrow)}$ (orange line) have the same P_β but different P_α in the circuit of Fig. 1 (b). As a result, the circuits for measuring these pairs involve exactly the same parameterized unitaries $U_G[\theta^1]$ and $U_t[\theta^2]$ in Fig. 1 (b), and therefore the same evolution of the number of CNOTs, circuit depth, and infidelity. However, the dynamics of these pairs in (a) and (b) are distinct due to different P_α .

CNOTs. The number of CNOTs increases rapidly up to $t \approx 3$ for the $N = 4$ simulations, before saturating at prolonged duration, while for the $N = 6$ simulations it exhibits a sublinear increase during the entire simulation

up to $t = 10$ for the $N = 6$ simulations. The number of CNOTs rises from the initial 270 (2402) for ground state preparation to a maximum number of 610 (6148) at the final simulation time of $t = 10$ for $N = 4$ ($N = 6$). The

resulting number of CNOTs at the final simulation time is comparable for the different components $I_{\alpha,\beta}^{p,q}$. In addition to the CNOT count and number of qubits, the circuit depth determined by the number of layers represents a critical metric for NISQ devices. Figures 2 (g) and 2 (h) present the evolution of the circuit depth with time for the $I_{\alpha,\beta}^{p,q}$ dynamics presented in Figs. 2 (a) and 2 (b). The depths of the state-preparation circuits are 26 and 147 for $N = 4$ and $N = 6$, respectively. During the time evolution, the circuit depth grows to a maximum of 65 (424) at the final simulation time of $t = 10$ for $N = 4$ ($N = 6$).

For comparison, if VQDS with HVA is used in the CUL Green's function calculations, the number of two-qubit rotation gates required for a single layer HVA is $8N^{3/2} + N - 4\sqrt{N}$ for the Fermi-Hubbard model with N sites and open boundary conditions [50]. For instance, with $N = 4$ and 16 layers of HVA as used in Ref. [50], the estimated number of two-qubit rotation gates is 960. Consequently, VQDS with a 16-layer HVA exceeds the maximum number of required CNOT gates of our AVQDS approach by approximately 50 %, despite yielding less accurate results at long simulation times compared to our results based on the AVQDS approach. This demonstrates that the calculations of the Green's function with AVQDS lead to much shallower quantum circuits relative to HVA. To compare with the CUR approach [61], we subtract the CNOTs in the ground state preparation circuit from the CNOT counts in Fig. 2 (e), as only the number of CNOTs accumulated during the time evolution is presented in Ref. [61]. After this adjustment, the maximum increase in the CNOT count during the time evolution is 340 within the studied time window of $[0, 10]$, which is about the same as that in Ref. [61]. We note that for the overlap test in CUR method, an additional $2N_p$ CNOTs are needed, which is about $2 \times 70 = 140$. Here N_p is the number of parameters introduced in the single-state AVQDS calculations in the CUR approach. Comparable CNOT counts but deeper quantum circuits are reported for CUR calculations using HVA for variational state propagation [55].

D. Momentum-space Green's function and spectral function

To further demonstrate the accuracy of CUL Green's function calculations using AVQDS, we study the retarded Green's function in momentum space, which has the following form:

$$G_{k,\sigma}^R = \frac{1}{N} \sum_{i,j=1}^N G_{(i,\sigma),(j,\sigma)}^R e^{-ik(i-j)}. \quad (17)$$

To calculate Eq. (17) using Eq. (11), $I_{\alpha,\beta}^{(i,\sigma),(j,\sigma)}(t)$ is evaluated for all i, j, σ, α , and β . In general, the t -stepping in the dynamics of $I_{\alpha,\beta}^{(i,\sigma),(j,\sigma)}(t)$ is not equidistant due to the dynamically adjusted δt in the AVQDS approach

and is also component-dependent. In practice, we obtain $I_{\alpha,\beta}^{(i,\sigma),(j,\sigma)}(t)$ on a uniform t -mesh using linear interpolation before calculating $G_{k,\sigma}^R$ via Eq. (17). For simplicity, we set $G_k^R \equiv G_{k,\sigma}^R$ due to spin rotation symmetry. Figures 3 (a) and 3 (b) show the real and imaginary parts of $G_k^R(t)$ at momentum $k = 0$ for Fermi-Hubbard chains with $N = 4$ - and $N = 6$ -sites, respectively. The real and imaginary parts of $G_{k=0}^R$ obtained with the AVQDS approach are shown as red circles and cyan diamonds, respectively, which agree well with the exact simulation results represented by solid black lines.

We next study the spectral function, which is defined by

$$A_k(\omega) = -\frac{1}{\pi} \text{Im} [G_k^R(\omega)], \quad (18)$$

where $G_k^R(\omega)$ is the Fourier transform of $G_k^R(t)$,

$$G_k^R(\omega) = \int_{-\infty}^{\infty} dt e^{i(\omega+i\varepsilon)t} G_k^R(t), \quad (19)$$

with infinitesimal ε to guarantee convergence of the integral. The calculation of Eq. (19) is challenging, as the accurate computation of the spectral function requires long simulation times. Here we adopt the Padé approximation for spectral analysis [61, 74], which has been demonstrated to accelerate the convergence of Fourier transforms with simulation time. To proceed, one first casts the discrete form of the Fourier transform (19) as a power series expansion:

$$G_k^R(\omega) = \sum_{n=0}^{N_T} G_k^R(t_n) z^n, \quad (20)$$

where $t_n = n\delta t$ is the n th point in a uniform time mesh $[0, T]$ with time step size $\delta t = T/N_T$ with N_T even, and $z^n = (e^{i(\omega+i\varepsilon)\delta t})^n$. We choose a diagonal Padé approximation [75], where $G_k^R(\omega)$ is expressed as a ratio of two polynomials of equal order:

$$G_k^R(\omega) = \frac{\sum_{n=0}^{N_T/2} a_n z^n}{1 + \sum_{n=1}^{N_T/2} b_n z^n}. \quad (21)$$

The coefficients of these polynomials, a_n and b_n , are obtained by solving the system of linear equations obtained from matching orders of z^n in Eqs. (20) and (21), as implemented in SciPy [76]. The resulting rational function (21) can then be used as an approximation to the original function. Since the coefficients are independent of frequency, $G_k^R(\omega)$ can be calculated for any frequency based on Eq. (21), in contrast to the Fast Fourier transform (FFT) where the spectral resolution is determined by the maximum simulation time t_{\max} . However, the accuracy of the Padé approximant depends on t_{\max} , as illustrated below.

Figures 3 (c) and 3 (d) show the spectral function $A_{k=0}(\omega)$ obtained by calculating the Fourier transform

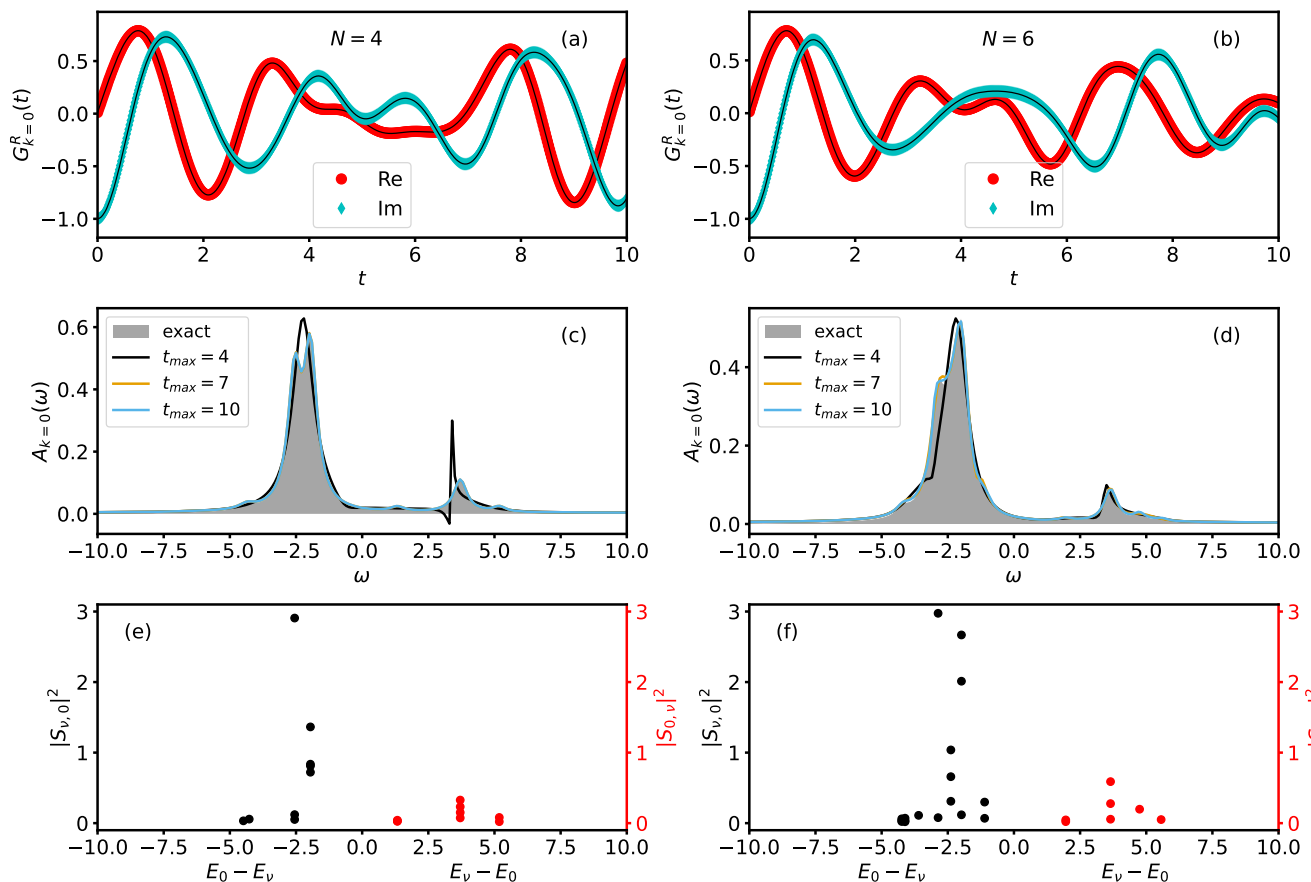


FIG. 3. **Single-particle Green's function in momentum space and spectral function.** Dynamics of the real and imaginary parts of $G_{k=0}^R(t)$ at momentum $k = 0$ for Fermi-Hubbard model with (a) $N = 4$ - and (b) $N = 6$ -sites. The real part (red circles) and imaginary part (cyan diamonds) of $G_{k=0}^R(t)$ obtained with the AVQDS approach agree well with the corresponding results of the exact simulations (solid black lines). (c), (d) Spectral function $A_{k=0}(\omega)$ obtained by Fourier transforming the dynamics presented in (a) and (b) using the Padé approximation and calculating Eq. (18). The result is shown for three different t_{\max} used within the Padé approximation. As a comparison, the exact result for the spectral function based on Eq. (22) is plotted as a shaded area. $t_{\max} = 7$ is sufficient to accurately reproduce the main features in $A_{k=0}(\omega)$. (e), (f) $|S_{\nu,0}|^2$ (black dots) and $|S_{0,\nu}|^2$ (red dots) as a function of the energy differences $E_0 - E_\nu$ and $E_\nu - E_0$, respectively, for (e) $N = 4$ and (f) $N = 6$. Only the dominant transition amplitudes with $|S_{\nu,\mu}|^2 > 0.02$ are shown. The peaks in the spectral functions originate from transitions between the ground state with energy E_0 to the excited states with energies E_ν , and vice versa.

of the real-time components presented in Figs. 3 (a) and 3 (b), using the Padé approximation with a damping factor of $\varepsilon = 0.3$ (tied to t_{\max}) and evaluating Eq. (18). The results are shown for three different values of t_{\max} used in the Padé approximation. For comparison, we also present the exact result for the spectral function (shaded area), obtained using the Lehmann representation of the Green's function, as derived in Appendix B. The simulated spectral function based on the AVQDS approach agrees well with the exact $A_{k=0}(\omega)$. In particular, a simulation time of $t_{\max} = 7$ is already sufficient to accurately reproduce the main features in $A_{k=0}(\omega)$ for the damping factor $\varepsilon = 0.3$ considered in the Fourier transformation (19). Compared to the discrete Fourier transform (20), the Padé approximation requires a smaller t_{\max} to accurately calculate the spectral function, as demonstrated in Ap-

pendix E.

To identify the origin of the peaks in the spectral function $A_{k=0}(\omega)$, we study the Lehmann representation of the Green's function in more detail. For $k = 0$, the Lehmann representation of the Green's function (B4) derived in Appendix B simplifies to

$$G_{k=0}^R(\omega) = \frac{1}{N} \sum_{\nu} \left[\frac{|S_{0,\nu}|^2}{E_0 - E_\nu + \omega + i\varepsilon} + \frac{|S_{\nu,0}|^2}{E_\nu - E_0 + \omega + i\varepsilon} \right],$$

$$S_{\nu,\mu} \equiv \sum_p M_{\nu,\mu}^p, \quad (22)$$

where $M_{\mu,\nu}^p \equiv \langle \Psi_\mu | \hat{c}_p | \Psi_\nu \rangle$ are the transition matrix elements between eigenstates $|\Psi_\nu\rangle$ and $|\Psi_\mu\rangle$ of the Hamil-

tonian (15). From this expression, it is evident that the peaks in the spectral function arise from transitions between the ground state with energy E_0 to the excited states with energies E_ν by adding an electron [first term in $G_{k=0}^R$ (22)] or removing an electron [second term in $G_{k=0}^R$ (22)], and vice versa. The spectral weight of these peaks in $A_{k=0}(\omega)$ is determined by $S_{\mu,\nu}$. Figures 3 (e) and 3 (f) present $|S_{\nu,0}|^2$ (black dots) and $|S_{0,\nu}|^2$ (red dots) as a function of the energy differences $E_0 - E_\nu$ and $E_\nu - E_0$, respectively, for $N = 4$ (Fig.3 (e)) and $N = 6$ (Fig.3 (f)). In the case of $N = 4$, the energetically close peaks around $\omega \approx -2.2$ in the spectral function in Fig. 3 (c) result from transitions between excited states $\nu = 7, \dots, 10$ to the ground state as well as from the transition of the $\nu = 12$ -state to the ground state. The excited states $\nu = 7, \dots, 10$ are degenerate with $E_0 - E_\nu = -1.955$ while $E_0 - E_{\nu=12} = -2.55$. The dominant signal at positive frequencies, $\omega \approx 3.7$, in Fig. 3 (c) results from transitions between the ground state and degenerate excited states $\nu = 11, \dots, 14$ with energy $E_\nu - E_0 = 3.71$. For $N = 6$, the peaks around $\omega \approx -2.5$ in the spectral function in Fig. 3 (d) stem from transitions between excited states $\nu = 18, 19$, $\nu = 25, 26, 27$, and $\nu = 40$ to the ground state. The excited states $\nu = 18, 19$ ($\nu = 25, 26, 27$) are degenerate with energy $E_0 - E_\nu = -1.98$ ($E_0 - E_\nu = -2.38$) while $E_0 - E_{\nu=40} = -2.87$. The dominant signal at positive frequencies, $\omega \approx 3.6$, in Fig. 3 (d) mainly results from transitions between the ground state and degenerate excited states $\nu = 41, 42, 43$ with energy $E_\nu - E_0 = 3.65$. As a result, the spectral function provides direct insights into the energy levels and excitations of fermions in the studied Fermi-Hubbard model.

V. COMPUTATION OF NONLINEAR SUSCEPTIBILITIES WITH AVQDS

A. Susceptibility expansion

We begin with a brief discussion of susceptibility expansion for the nonlinear responses measured in 2DCS experiments. We consider an N -site quantum spin system described by spin- s operators \hat{S}_i^p ($p = x, y, z$) at site i . The transmitted magnetic field measured in 2DCS experiments on magnetic systems is determined by the magnetization $\mathbf{M}(t) \equiv \langle \hat{\mathbf{S}}^{\text{tot}} \rangle = \langle \Psi[t] | \hat{\mathbf{S}}^{\text{tot}} | \Psi[t] \rangle$. Here, $\hat{\mathbf{S}}^{\text{tot}} = \sum_{j=1}^N \hat{\mathbf{S}}_j$ is the total spin operator and $|\Psi[t]\rangle$ corresponds to the quantum state of the system at time t . In 2DCS the quantum spin system is excited by two magnetic field pulses polarized along the β - and γ -directions, separated in time by τ . The total applied magnetic field can be written as $\mathbf{B}(t) = B_1^\beta(t)\boldsymbol{\beta} + B_2^\gamma(t-\tau)\boldsymbol{\gamma}$, with the two pulses centered at time $t = 0$ and $t = \tau$, while $\boldsymbol{\beta}$ and $\boldsymbol{\gamma}$ denote the unit vectors along the β and γ directions. The differential transmitted magnetic field along the α direction, B_{NL}^α , as measured in 2DCS experiments, is

proportional to the nonlinear differential magnetization:

$$M_{\text{NL}}^\alpha(t, \tau) = M_{12}^\alpha(t, \tau) - M_1^\alpha(t) - M_2^\alpha(t, \tau), \quad (23)$$

which depends on time t and the inter-pulse delay τ . Here, $M_{12}^\alpha(t, \tau)$ denotes the magnetization dynamics induced by both pulses, while $M_1^\alpha(t)$ and $M_2^\alpha(t, \tau)$ denote the magnetization dynamics induced by pulses 1 and 2, respectively. As demonstrated in Ref. [62], the 2DCS spectra obtained by a 2D Fourier transform of Eq. (23) can be interpreted by applying a susceptibility expansion [3–5] of $M_{\text{NL}}^\alpha(t, \tau)$. By approximating the pulse shapes by δ -functions, the applied magnetic field can be written as

$$\mathbf{B}(t) = A_1^\beta \delta(t)\boldsymbol{\beta} + A_2^\gamma \delta(t-\tau)\boldsymbol{\gamma}, \quad (24)$$

where A_i corresponds to the i th pulse area. As a result, the nonlinear magnetization density along the α -direction at time $t + \tau$ can be expressed in terms of nonlinear susceptibilities $\chi^{(n)}$ of order n [4, 5, 77]:

$$\begin{aligned} & M_{\text{NL}}^\alpha(t + \tau)/N \\ & \equiv (M_{12}^\alpha(t + \tau) - M_1^\alpha(t + \tau) - M_2^\alpha(t + \tau))/N \\ & = \chi_{\alpha\beta\gamma}^{(2)}(t, \tau) A_1^\beta A_2^\gamma \\ & + \chi_{\alpha\beta\gamma\delta}^{(3)}(t, \tau, 0) (A_1^\beta)^2 A_2^\gamma + \chi_{\alpha\beta\gamma\delta}^{(3)}(t, 0, \tau) A_1^\beta (A_2^\gamma)^2 \\ & + \mathcal{O}(B^4). \end{aligned} \quad (25)$$

The second-order susceptibility in the above equation is explicitly given by [4, 77]

$$\begin{aligned} & \chi_{\alpha\beta\gamma}^{(2)}(t, \tau) = \\ & - \frac{1}{N} \Theta(t)\Theta(\tau) \langle \left[\left[\hat{M}^\alpha(t + \tau), \hat{M}^\beta(\tau) \right], \hat{M}^\gamma(0) \right] \rangle, \end{aligned} \quad (26)$$

while the third-order susceptibilities are defined by [5]

$$\begin{aligned} & \chi_{\alpha\beta\gamma\delta}^{(3)}(t, \tau, 0) = \\ & - \frac{i}{N} \Theta(t)\Theta(\tau) \langle \left[\left[\left[\hat{M}^\alpha(t + \tau), \hat{M}^\beta(\tau) \right], \hat{M}^\gamma(0) \right], \hat{M}^\delta(0) \right] \rangle, \end{aligned} \quad (27)$$

$$\begin{aligned} & \chi_{\alpha\beta\gamma\delta}^{(3)}(t, 0, \tau) = \\ & - \frac{i}{N} \Theta(t)\Theta(\tau) \langle \left[\left[\left[\hat{M}^\alpha(t + \tau), \hat{M}^\beta(\tau) \right], \hat{M}^\gamma(\tau) \right], \hat{M}^\delta(0) \right] \rangle. \end{aligned} \quad (28)$$

In this paper, we demonstrate the calculation of the third-order susceptibility $\chi_{\alpha\beta\gamma\delta}^{(3)}(t, \tau, 0)$ using a quantum computing approach. The second-order $\chi_{\alpha\beta\gamma}^{(2)}(t, \tau)$ and third-order $\chi_{\alpha\beta\gamma\delta}^{(3)}(t, 0, \tau)$ as well as higher-order susceptibilities can be evaluated similarly. This approach is complementary to the method of direct observable dynamics simulations we developed earlier by disentangling contributions from quantum processes of different orders [62].

B. Formalism

We next discuss how $\chi_{\alpha\beta\gamma\delta}^{(3)}(t, \tau, 0)$ can be measured on a quantum computer. By using $\hat{M}^\alpha = \sum_{j=1}^N \hat{S}_j^\alpha$, the third-order susceptibility (27) can be written as:

$$\begin{aligned} \chi_{\alpha\beta\gamma\delta}^{(3)}(t, \tau, 0) &= \frac{2}{N} \Theta(t)\Theta(\tau) \sum_{j,k,l,m=1}^N \text{Im} \left[\langle \hat{S}_j^\alpha(t+\tau) \hat{S}_k^\beta(\tau) S_l^\gamma(0) S_m^\delta(0) \rangle \right. \\ &\quad + \langle S_m^\delta(0) S_l^\gamma(0) \hat{S}_j^\alpha(t+\tau) \hat{S}_k^\beta(\tau) \rangle \\ &\quad - \langle \hat{S}_l^\gamma(0) \hat{S}_j^\alpha(t+\tau) \hat{S}_k^\beta(\tau) S_m^\delta(0) \rangle \\ &\quad \left. - \langle \hat{S}_l^\delta(0) \hat{S}_j^\alpha(t+\tau) \hat{S}_k^\beta(\tau) S_m^\gamma(0) \rangle \right]. \end{aligned} \quad (29)$$

To evaluate Eq. (29) for a generic spin- s model using a quantum computer, one can either use a qudit-based quantum device [78, 79] or bosonic quantum devices [80, 81] where the number of qudit levels/qumodes corresponds to the number of spin states $2s + 1$, or map the spin- s levels to qubits using transformations such as the Gray code or binary encoding [62, 82]. In this paper, we choose the latter approach as qubit-based platforms are currently the most widely available. The transformation of spin- s operators to multi-qubit operators can be written as

$$\hat{S}_j^\alpha = \sum_{p=1}^{n_\alpha} \eta_{j,p}^\alpha P_{j,p}^\alpha. \quad (30)$$

Here, the transformation contains n_α terms and the index $j = 1, \dots, N$ labels the physical site; $\eta_{j,p}^\alpha$ are real-valued coefficients and $P_{j,p}^\alpha$ are Pauli words. The encoding of a spin- s site requires n_q qubits such that the system contains $N_q = n_q N$ qubits in total. Using $\hat{S}_j^\alpha(t) = e^{i\hat{H}t} \hat{S}_j^\alpha e^{-i\hat{H}t}$ and Eq. (30), Eq. (29) becomes

$$\begin{aligned} \chi_{\alpha\beta\gamma\delta}^{(3)}(t, \tau, 0) &= \frac{2}{N} \Theta(t)\Theta(\tau) \sum_{j,k,l,m=1}^N \sum_{p=1}^{n_\alpha} \sum_{q=1}^{n_\beta} \sum_{r=1}^{n_\gamma} \sum_{s=1}^{n_\delta} \eta_{j,p}^\alpha \eta_{k,q}^\beta \eta_{l,r}^\gamma \eta_{m,s}^\delta \\ &\times \text{Im} \left[\langle e^{i\hat{H}(t+\tau)} P_{j,p}^\alpha e^{-i\hat{H}t} P_{k,q}^\beta e^{-i\hat{H}\tau} P_{l,r}^\gamma P_{m,s}^\delta \rangle \right. \\ &\quad + \langle P_{m,s}^\delta P_{l,r}^\gamma e^{i\hat{H}(t+\tau)} P_{j,p}^\alpha e^{-i\hat{H}t} P_{k,q}^\beta e^{-i\hat{H}\tau} \rangle \\ &\quad - \langle P_{l,r}^\gamma e^{i\hat{H}(t+\tau)} P_{j,p}^\alpha e^{-i\hat{H}t} P_{k,q}^\beta e^{-i\hat{H}\tau} P_{m,s}^\delta \rangle \\ &\quad \left. - \langle P_{l,r}^\delta e^{i\hat{H}(t+\tau)} P_{j,p}^\alpha e^{-i\hat{H}t} P_{k,q}^\beta e^{-i\hat{H}\tau} P_{m,s}^\gamma \rangle \right]. \end{aligned} \quad (31)$$

All the terms in Eq. (31) can be measured using the circuit in Fig. 4 (a). Nevertheless, to reduce the circuit depth for near-term applications, we adopt the generalized CUL circuit shown in Fig. 4 (b) for nonlinear correlation function simulations. In the CUL circuit, the state propagation for the system plus ancilla due to $e^{-i\hat{H}\tau}$ maps to the evolution of parameters in $U_G[\boldsymbol{\theta}^1]$

and $U_\tau[\boldsymbol{\theta}^3]$; while the state propagation due to $e^{-i\hat{H}t}$ maps to parameter updating in $U_G[\boldsymbol{\theta}^1]$, $U_\tau[\boldsymbol{\theta}^3]$, and $U_t[\boldsymbol{\theta}^2]$. We adopt AVQITE to generate $U_G[\boldsymbol{\theta}^1]$ for ground state preparation, and AVQDS to generate $U_\tau[\boldsymbol{\theta}^3]$ and $U_t[\boldsymbol{\theta}^2]$ for state evolution. More detailed discussions are given in Appendix C on measuring the different terms within the square brackets of Eq. (31) using the CUL circuit in Fig. 4 (b). Specifically, the CUL circuit measures the imaginary part of $\langle G[\boldsymbol{\theta}^1] | P_0 P_1 U_\tau^\dagger[\boldsymbol{\theta}^3] U_t^\dagger[\boldsymbol{\theta}^2] P_2 U_t[\boldsymbol{\theta}^2] P_3 U_\tau[\boldsymbol{\theta}^3] P_4 P_5 | G[\boldsymbol{\theta}^1] \rangle$. By setting $P_0 = P_1 = I^{\otimes N_q}$, $P_2 = P_{j,p}^\alpha$, $P_3 = P_{k,q}^\beta$, $P_4 = P_{l,r}^\gamma$, and $P_5 = P_{m,s}^\delta$ ($P_0 = P_{m,s}^\delta$, $P_1 = P_{l,r}^\gamma$, $P_2 = P_{j,p}^\alpha$, $P_3 = P_{k,q}^\beta$, and $P_4 = P_5 = I^{\otimes N_q}$), the first (second) term within the square brackets of Eq. (31) is calculated, while the third (fourth) contributions follow by setting $P_0 = P_5 = I^{\otimes N_q}$, $P_1 = P_{l,r}^{\gamma(\delta)}$, $P_2 = P_{j,p}^\alpha$, $P_3 = P_{k,q}^\beta$, and $P_4 = P_{m,s}^{\delta(\gamma)}$. We note that the CUL circuit in Fig. 4 (b) can be simplified for specific settings of $\{P_i\}_{i=0}^5$ gates. For instance, if Pauli gate $P_i = I^{\otimes N_q}$, it can be removed trivially. If $P_4 = P_0$, the two controlled P_4 and P_0 gates can be merged to a single P_0 gate.

The calculation of the different terms of Eq. (31) involves four main steps: (i) Preparation of the ground state of the quantum spin Hamiltonian, $|G[\boldsymbol{\theta}^1]\rangle = U_G[\boldsymbol{\theta}^1]|\varphi_0\rangle$ where $|\varphi_0\rangle$ is a reference product state, using adaptive variational algorithms like qubit ADAPT-VQE [69] or AVQITE [59]. This step is analogous to step (i) for the calculation of the Green's function using the quantum circuit in Fig. 1 (b). (ii) Generating and evolving the parameterized unitary circuit $U_\tau(\boldsymbol{\theta}^3(\tau))$ by applying the AVQDS approach discussed in Sec. II to propagate the quantum state

$$\begin{aligned} |\Psi\rangle &= \frac{1}{\sqrt{2}} \left[|1\rangle \otimes P_1 P_0 |G[\boldsymbol{\theta}^1(\tau)]\rangle \right. \\ &\quad \left. + i |0\rangle \otimes P_4 P_5 |G[\boldsymbol{\theta}^1(\tau)]\rangle \right], \end{aligned} \quad (32)$$

where the parameters $\boldsymbol{\theta}^1(\tau)$ also evolve from the ground state solution to leverage their degrees of freedom for dynamics simulations. Here, Eq. (32) corresponds to the state in the circuit in Fig. 4 (b) after applying the controlled P_1 operation. (iii) Generating and evolving the parameterized unitary circuit $U_t(\boldsymbol{\theta}^2(t))$ by applying the AVQDS approach to propagate the state

$$\begin{aligned} |\Psi\rangle &= \frac{1}{\sqrt{2}} \left[|0\rangle \otimes U_\tau(\boldsymbol{\theta}^3(t)) P_1 P_0 |G[\boldsymbol{\theta}^1(t)]\rangle \right. \\ &\quad \left. + i |1\rangle \otimes P_3 U_\tau(\boldsymbol{\theta}^3(t)) P_4 P_5 |G[\boldsymbol{\theta}^1(t)]\rangle \right], \end{aligned} \quad (33)$$

where $\boldsymbol{\theta}^1(t)$ and $\boldsymbol{\theta}^3(t)$ also vary to facilitate the state propagation using compact circuits. (iv) Repeat the quantum circuit evaluations in Fig. 4 (b) for the different contributions in Eq. (31), which in total involves $4N^4 n_\alpha n_\beta n_\gamma n_\delta$ terms.

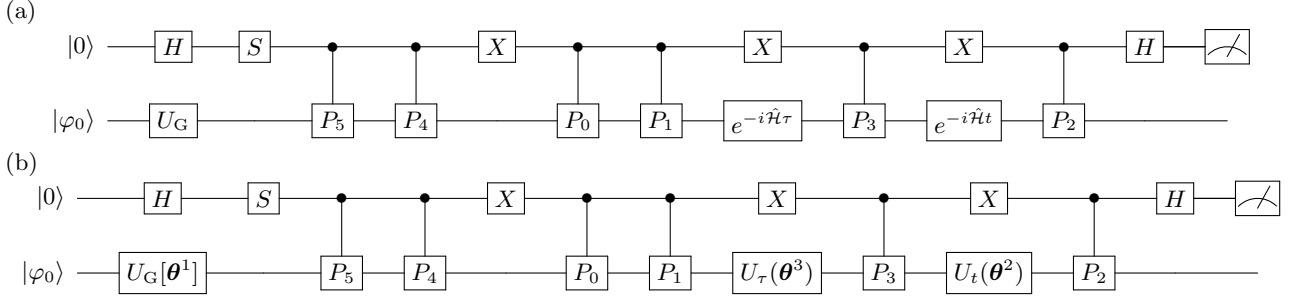


FIG. 4. **Quantum circuit for measuring the third-order susceptibility (31).** (a) Circuit utilizing exact time-evolution gates. The upper horizontal line represents the ancillary qubit, initially in the state $|0\rangle$. X , H , and S correspond to the Pauli- X , Hadamard rotation, and S -gate operations on the ancilla. The lower horizontal line denotes the qubit register representing the quantum spin system, initially in a reference product state $|\varphi_0\rangle$, which is rotated to the ground state $|G\rangle = U_G |\varphi_0\rangle$ by a unitary circuit U_G . Multiple controlled Pauli gates are used to measure different terms in Eq. (31). The expectation value $\text{Im}[\langle G| P_0 P_1 e^{i\hat{H}(t+\tau)} P_2 e^{-i\hat{H}t} P_3 e^{-i\hat{H}\tau} P_4 P_5 |G\rangle]$ is obtained by Pauli- Z measurement on the ancilla qubit. (b) The CUL circuit to measure the third-order susceptibility, which is an adaptive variational circuit equivalent to (a). The ground state is prepared using a parameterized circuit $U_G[\theta^1]$, the state propagation by $e^{-i\hat{H}\tau}$ is achieved by evolving the angles in $U_\tau[\theta^3]$ and $U_G[\theta^1]$, and state propagation by $e^{-i\hat{H}t}$ is achieved by evolving angles in $U_t[\theta^2]$, $U_\tau[\theta^3]$, and $U_G[\theta^1]$. The parameterized unitaries $U_G[\theta^1]$, $U_t[\theta^2]$, and $U_\tau[\theta^3]$ are automatically generated using adaptive variational algorithms.

VI. THIRD-ORDER SUSCEPTIBILITY OF TWO-SITE QUANTUM SPIN-1 MODEL

A. Model

To demonstrate the calculation of the third-order susceptibility using the CUL circuit presented in Sec. VI, we investigate a higher-spin model that has been used to describe 2DCS experiments on rare-earth orthoferrites [62]. The Hamiltonian is given by:

$$\hat{H} = J \sum_{i=1}^{N-1} \hat{\mathbf{S}}_i \cdot \hat{\mathbf{S}}_{i+1} - \mathbf{D} \cdot \sum_{i=1}^{N-1} \hat{\mathbf{S}}_i \times \hat{\mathbf{S}}_{i+1}. \quad (34)$$

The first term of the Hamiltonian characterizes the anti-ferromagnetic coupling between nearest neighbors with an exchange constant $J > 0$. The second term in Eq. (34) describes the Dzyaloshinskii-Moriya (DM) interaction with an antisymmetric exchange vector \mathbf{D} , which we assume to be aligned along the y -direction, i.e., $\mathbf{D} = D\mathbf{y}$.

In the simulations, we consider a two-site spin-1 model for demonstration. Note that the quantum resource scaling with respect to system size and spin magnitude s for the ground state and dynamics simulations of this model have been numerically studied in Refs. [62, 82]. We define the energy unit by setting the coupling constant J to one, while using a Dzyaloshinskii-Moriya interaction strength of $D = 0.2$. The inset of Fig. 5(e) shows the energy levels E_n of the analyzed two-site spin-1 model obtained via exact diagonalization. The energy difference between the ground state ($n = 0$) and the first excited state ($n = 1$) determines the magnon frequency $\omega_{\text{AF}} = E_1 - E_0 \approx 0.16$, represented by the double arrow. Notably, the eigenenergies of states $n = 1, 2, 3$ as well as the states $n = 4, \dots, 8$ are nearly degenerate and the energy difference between $E_{n=1,2,3}$ and $E_{n=4,\dots,8}$ is approximately $2\omega_{\text{AF}}$ (see inset

of Fig. 5), indicating a quasi-harmonic energy spectrum of the two-site spin-1 model, as discussed in more detail in Ref. [62].

To map the spin-1 operators to multi-qubit operators, we use the Gray code [83] which provides shallower quantum circuits compared to the binary encoding in calculating two-dimensional coherent spectra, as demonstrated in Ref. [62]. The encoding of the spin-1 operators requires $n_q = 2$ qubits for a single spin such that the Hamiltonian (34) for $N = 2$ sites is represented by $N_q = n_q N = 4$ qubits.

B. Ground state preparation

To prepare the ground state $|G\rangle$ of the quantum-spin Hamiltonian (34), we employ the AVQITE method [59]. We utilize $|\varphi_0\rangle = |0\rangle^{\otimes N_q}$ as our reference state. For the ground state preparation, we adopt the following operator pool:

$$\mathcal{P} = \{\sigma_i^y\}_{i=1}^{N_q} \cup \{\sigma_i^y \sigma_{i+1}^z\}_{i=1}^{N_q-1} \cup \{\sigma_i^z \sigma_{i+1}^y\}_{i=1}^{N_q-1}. \quad (35)$$

For the third-order susceptibility calculation with AVQDS, we utilize the following pool:

$$\begin{aligned} \mathcal{P} = & \{A_i : A \in \{\sigma^x, \sigma^y, \sigma^z\}, 1 \leq i \leq N_q\} \\ & \cup \{A_i B_j : A, B \in \{\sigma^x, \sigma^y, \sigma^z\}, 1 \leq i < j \leq N_q\}. \end{aligned} \quad (36)$$

This pool contains all possible one- and two-qubit Pauli words.

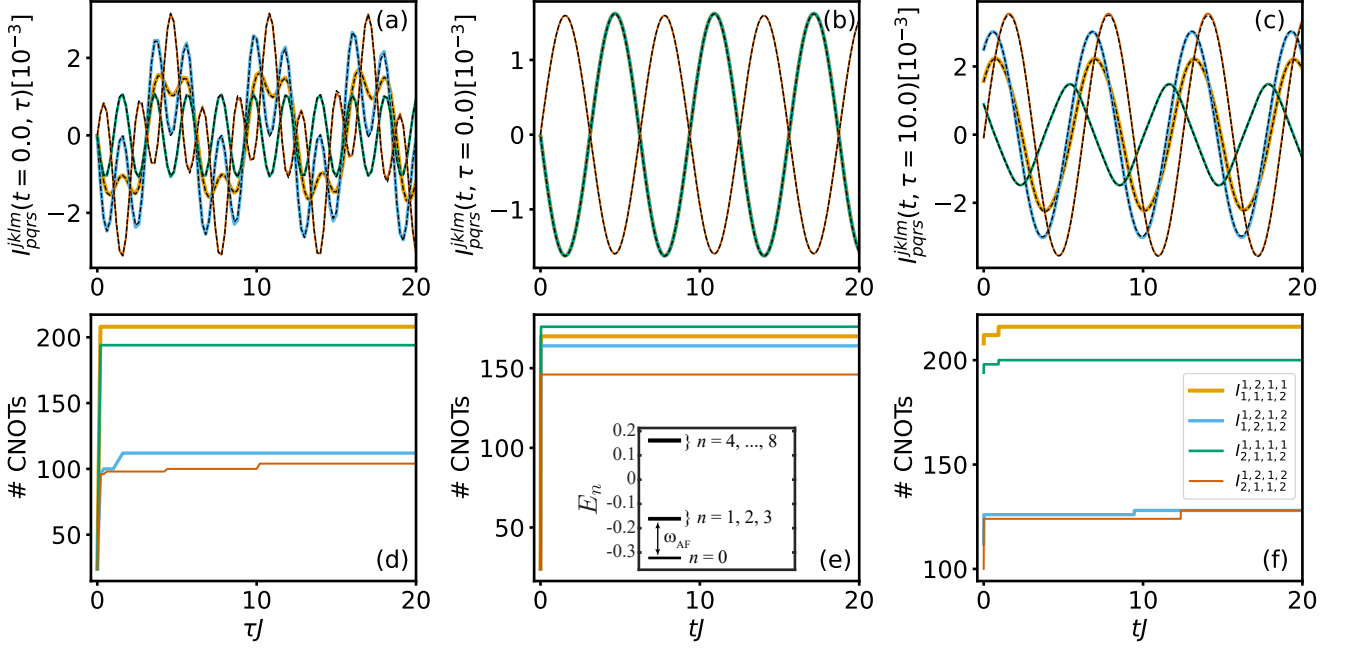


FIG. 5. Numerical simulation of the AVQDS algorithm for calculating the third-order nonlinear susceptibility of the two-site spin-1 model. (a)–(c) Four examples of $I_{pqrs}^{jklm}(t, \tau)$ (a) as a function of τ at fixed $tJ = 0$, and as a function of time t at fixed (b) $\tau J = 0$ and (c) $\tau J = 10$. The dynamics obtained by the AVQDS approach (solid lines) accurately reproduce the exact dynamics (dashed black lines) for all presented I_{pqrs}^{jklm} . (d)–(f) The corresponding dynamics of the required number of CNOT gates. The number of CNOT gates significantly increases only at earlier times and saturates after a time of about $\tau J = 1.5$ in (d) and $tJ = 1.3$ in (e) and (f). The saturated number of CNOTs at the final simulation time of $tJ = 20$ falls within the range of 128 to 216. Inset of (e): Eigenenergies E_n of the quantum spin Hamiltonian in Eq. (34). The Hamiltonian exhibits $(2s + 1)^N = 9$ eigenstates for $N = 2$ sites and spin- $s = 1$. The magnon frequency $\omega_{AF} = E_1 - E_0 \approx 0.16$ is given by the energy difference between the ground state ($n = 0$) and the first excited state ($n = 1$). The states $n = 1, 2, 3$ as well as $n = 4, \dots, 8$ are nearly degenerate.

C. Simulation results

To demonstrate the calculation of the third-order susceptibility using the CUL circuits with AVQDS presented in Sec. VB, we focus on the third-order susceptibility $\chi_{zzzz}^{(3)}(t, \tau, 0)$. This susceptibility is particularly relevant for analyzing 2DCS experiments employing a collinear two-pulse geometry, where the applied magnetic field consists of two copropagating pulses polarized along the z -direction. In such a scenario, the third and fourth terms within the square brackets in Eq. (31) become identical. Since the transformation (30) involves $n_z = 2$ terms for \hat{S}_j^z and spin $s = 1$ [62], the summation in Eq. (31) encompasses $3N^4 n_z^4 = 768$ terms, each of which needs to be calculated using the CUL circuit depicted in Fig. 4 (b).

To illustrate the calculation of $\chi_{zzzz}^{(3)}(t, \tau, 0)$ with the CUL circuit in Fig. 4 (b), we use the first term within the

square brackets of Eq. (31) as an example:

$$\begin{aligned}
 & I_{pqrs}^{jklm}(t, \tau) \\
 & \equiv \text{Im}[\langle e^{i\hat{H}(t+\tau)} P_{j,p}^z e^{-i\hat{H}t} P_{k,q}^z e^{-i\hat{H}\tau} P_{l,r}^z P_{m,s}^z \rangle] \\
 & \approx \text{Im}[\langle G[\theta^1] | U_\tau^\dagger(\theta^2) U_t^\dagger(\theta^3) P_{j,p}^z U_t(\theta^3) P_{k,q}^z \\
 & \quad \times U_\tau(\theta^2) P_{l,r}^z P_{m,s}^z | G[\theta^1] \rangle]. \quad (37)
 \end{aligned}$$

We first evolve the state in Eq. (32) with $P_0 = P_1 = I^{\otimes N_q}$, $P_4 = P_{l,r}^z$, and $P_5 = P_{m,s}^z$ up to time τ using AVQDS. After applying the X -gate and controlled $P_3 = P_{k,q}^z$ gate, we further propagate the state in Eq. (33) to $t \in [0, t_{\max}]$, for which we adopt a uniform time mesh. Similar circuit simulations are repeated for $\tau \in [0, \tau_{\max}]$ with a uniform mesh.

Figure 5 (a) shows four examples of $I_{pqrs}^{jklm}(t, \tau)$ as a function of τ at fixed $t = 0$, while Figs. 5 (b) and 5 (c) present the corresponding $I_{pqrs}^{jklm}(t, \tau)$ as a function of t at fixed $\tau = 0$ and $\tau J = 10$, respectively. The results obtained from the AVQDS approach (solid lines) are compared with the exact simulation results obtained by evolving the states in Eqs. (32) and (33) using exact diagonalization (8) (dashed black lines). The results from

the CUL circuit simulations agree with the exact dynamics for all presented I_{pqrs}^{ijklm} , with fidelities exceeding 99.99%.

The corresponding number of CNOT gates as a function of time are shown in Figs. 5 (d)–5 (f). The initial 22 CNOTs at $t = \tau = 0$ are determined by the ground state ansatz, which is obtained using qubit-ADAPT-VQE with an infidelity of about 10^{-10} . Throughout the time evolution, the number of CNOT gates only increases rapidly at very early times, followed by saturation after a time of about $\tau J = 1.5$ (Fig. 5 (d)) and $tJ = 1.3$ (Figs. 5 (e) and 5 (f)). The saturated number of CNOTs at the final simulation time of $tJ = 20$ ranges from 128 to 216 for the various $I_{pqrs}^{ijklm}(t, \tau)$.

To obtain the third-order susceptibility $\chi_{zzzz}^{(3)}(t, \tau, 0)$, we simulated the different contributions in Eq. (31) using the CUL circuit in Fig. 4 (b). Simulations were performed up to $\tau_{\max} J = 40$ with a step size of $\delta\tau = 0.5$, which provides sufficient resolution of the signals in the 2D spectrum of the third-order susceptibility. To calculate $\chi_{zzzz}^{(3)}(t, \tau, 0)$, we interpolated the different contributions in Eq. (31) to a 401×401 uniform mesh of t and τ with $t_{\max} J = \tau_{\max} J = 40$ before performing the summation over the components in Eq. (31). Figure 6 (a) shows $\chi_{zzzz}^{(3)}(t, \tau, 0)$ as a function of times t and τ from statevector simulations of the CUL circuits. The corresponding result for the exact dynamics, derived in Appendix D, is presented in Fig. 6 (b). The third-order susceptibility obtained by the CUL circuits agrees well with the exact simulation result. This is further demonstrated by the slices at fixed τ and fixed t plotted in Figs. 6 (c) and 6 (d), where the CUL circuit results (circles) match the exact result (solid black line) over the full range of simulation times.

Figures 6 (e) and 6 (f) show the resulting 2D spectra of the third-order susceptibility, $\chi_{zzzz}^{(3)}(\omega_t, \omega_\tau, 0)$, obtained after performing the 2D discrete Fourier transformation of $\chi_{zzzz}^{(3)}(t, \tau, 0)$ from Figs. 6 (a) and 6 (b) using the Padé approximation in both the t and τ -directions. The 2D spectrum of the third-order susceptibility transformed from the real-time CUL circuit results agrees well with that from ED. The 2D spectrum exhibits four dominant peaks at $(\omega_t, \omega_\tau) = (0, \pm\omega_{\text{AF}})$, $(\omega_t, \omega_\tau) = (0, 0)$, and $(\omega_t, \omega_\tau) = (\omega_{\text{AF}}, \omega_{\text{AF}})$. As demonstrated in Ref. [62] and discussed in Appendix D, these signals originate from transitions between the ground state $|\Psi_0\rangle$ and the first excited state $|\Psi_1\rangle$, as well as between $|\Psi_1\rangle$ and the third excited state $|\Psi_3\rangle$. Such signals directly manifest in the 2DCS spectra, underscoring the significance of nonlinear susceptibilities in interpreting 2DCS experiments.

VII. CONCLUSION AND OUTLOOK

In this work, we presented and benchmarked quantum computing methods to calculate single-particle Green's functions and nonlinear susceptibilities, adopting controlled-unitaries-liberated circuits and adaptive variational algorithms for ground state preparation and real-

time propagation. For the computation of single-particle Green's functions, we followed the CUL approach outlined in Ref. [50], utilizing AVQITE to generate ground state circuits and AVQDS to approximate the time-evolution operator instead of CUL with HVA as in Ref. [50]. To illustrate the CUL approach, we computed the single-particle Green's function of Fermi-Hubbard chains with $N = 4$ and $N = 6$ sites. Specifically, we evaluated the real-time Green's function in momentum space as well as its corresponding spectral function, and compared the results with exact diagonalization calculations using the Lehmann representation of the Green's function. Our findings demonstrate that the CUL approach with AVQDS can accurately simulate the dynamics of Green's functions over sufficiently long times and obtain reliable spectral functions using the Padé approximation. The CUL quantum circuits required for the simulation of the Green's functions are shallower compared to those obtained with HVA in Ref. [50]. Furthermore, in comparison to the calculation of the single-particle Green's function with the CUR method using AVQDS in Ref. [61], our results demonstrate that utilizing the CUL approach with AVQDS can reduce the circuit complexity by bypassing the state overlap measurement. Comparable CNOT counts but deeper quantum circuits are required for CUR with HVA [55].

We also extended the CUL method from calculating single-particle Green's functions to evaluating nonlinear susceptibilities, which is crucial to explain the two-dimensional coherent spectroscopy experiments. Here, the nonlinear susceptibilities depend on two times such that their computation via the quantum circuit presented in Fig. 4 (b) requires the application of the AVQDS algorithm for two times. To demonstrate the validity of our method, we studied an antiferromagnetic quantum spin model including a Dzyaloshinskii-Moriya interaction. We calculated the third-order nonlinear susceptibility in the 2D time and frequency domains for a two-site spin-1 model and compared the results with numerical exact data. The third-order susceptibility calculated using the quantum computing approach agrees well with the exact result which confirms the accuracy of the CUL method in evaluating higher-order correlation functions using AVQDS for state evolution.

The presented algorithms for computing single-particle Green's functions and nonlinear susceptibilities can readily be extended to calculate higher-order multi-time correlation functions that depend on more than two times. Here, it would be interesting to compare the quantum resources required by the CUL method used in this paper against those required by the CUR approach considered in Refs. [55, 61]. Regarding the practical implementation of the AVQDS approach for computing high-order correlation functions on quantum hardware, it is essential to investigate the impact of hardware noise and shot noise resulting from a finite number of measurements. Here, the incorporation of error mitigation methods plays a crucial role [84, 85].

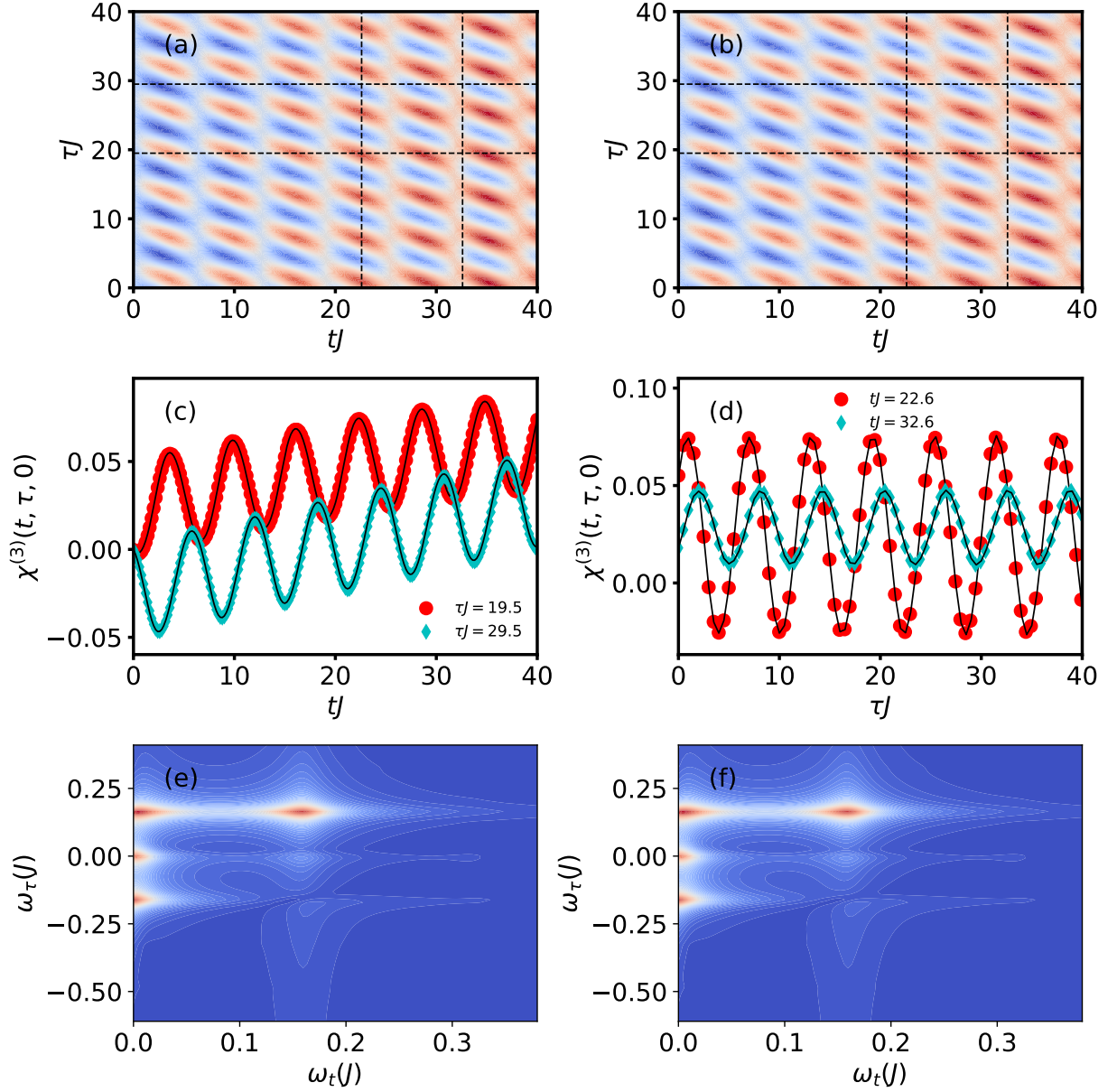


FIG. 6. **Third-order susceptibility of the two-site spin-1 system in the two-dimensional time and frequency domains.** (a) $\chi_{zzzz}^{(3)}(t, \tau, 0)$ as a function of times t and τ calculated using the CUL circuit, which agrees with the exact result in (b) obtained by evaluating Eq. (D1). Slices shown in (c) and (d) are indicated by horizontal and vertical dashed lines. (c), (d) Slices of $\chi_{zzzz}^{(3)}(t, \tau, 0)$ from (a) and (b) at two fixed times τ (c) and t (d). The AVQDS results (circles) accurately reproduce the exact dynamics (solid black lines). (e), (f) Two-dimensional (2D) Fourier transform of $\chi_{zzzz}^{(3)}(t, \tau, 0)$ from (a) and (b), respectively. Both 2D spectra are in excellent agreement.

ACKNOWLEDGEMENTS

We acknowledge useful discussions with P. P. Orth and N. Gomes. This work was supported by the U.S. Department of Energy (DOE), Office of Science, Basic Energy Sciences, Materials Science and Engineering Division, including the grant of computer time at the National Energy Research Scientific Computing Center (NERSC)

in Berkeley, California. The research was performed at the Ames National Laboratory, which is operated for the U.S. DOE by Iowa State University under Contract No. DE-AC02-07CH11358.

Appendix A: Quantum circuit for calculating single-particle Green's functions

In this appendix, we demonstrate that the quantum circuit in Fig. 1 (b) evaluates Eq. (14). The system qubits are initialized in a reference product state $|\varphi_0\rangle$, which can be straightforwardly prepared on a quantum computer. Then, the ground state is prepared by applying the unitary operator $U_G[\boldsymbol{\theta}^1]$ following AVQITE, yielding $|G[\boldsymbol{\theta}^1]\rangle = U_G[\boldsymbol{\theta}^1]|\varphi_0\rangle$. The initial state of the ancilla qubit is $|0\rangle$, which becomes $(|0\rangle + |1\rangle)/\sqrt{2}$ after applying the Hadamard gate. The quantum state after applying U_G on the system qubits and H on the ancilla qubit reads:

$$|\Psi\rangle = \frac{1}{\sqrt{2}} [|0\rangle \otimes |G[\boldsymbol{\theta}^1]\rangle + |1\rangle \otimes |G[\boldsymbol{\theta}^1]\rangle]. \quad (\text{A1})$$

After applying the controlled P_β operation controlled by the ancilla qubit, the state is given by $\frac{1}{\sqrt{2}} |0\rangle \otimes |G\rangle + \frac{1}{\sqrt{2}} |1\rangle \otimes P_\beta |G\rangle$. The time-evolving state under AVQDS with time-dependent parameters $\boldsymbol{\theta}^1(t)$ and $\boldsymbol{\theta}^2(t)$ becomes:

$$\begin{aligned} |\Psi\rangle &= \frac{1}{\sqrt{2}} |0\rangle \otimes U_t[\boldsymbol{\theta}^2] |G[\boldsymbol{\theta}^1]\rangle \\ &+ \frac{1}{\sqrt{2}} |1\rangle \otimes U_t[\boldsymbol{\theta}^2] P_\beta |G[\boldsymbol{\theta}^1]\rangle. \end{aligned} \quad (\text{A2})$$

Applying the X -gate on the ancilla qubit followed by the controlled P_α operation yields

$$\begin{aligned} |\Psi\rangle &= \frac{1}{\sqrt{2}} |1\rangle \otimes P_\alpha U_t[\boldsymbol{\theta}^2] |G[\boldsymbol{\theta}^1]\rangle \\ &+ \frac{1}{\sqrt{2}} |0\rangle \otimes U_t[\boldsymbol{\theta}^2] P_\beta |G[\boldsymbol{\theta}^1]\rangle. \end{aligned} \quad (\text{A3})$$

After the application of the Hadamard gate on the ancilla, the quantum state is given by

$$\begin{aligned} |\Psi\rangle &= \frac{1}{2} |0\rangle \otimes (P_\alpha U_t[\boldsymbol{\theta}^2] + U_t[\boldsymbol{\theta}^2] P_\beta) |G[\boldsymbol{\theta}^1]\rangle \\ &- \frac{1}{2} |1\rangle \otimes (P_\alpha U_t[\boldsymbol{\theta}^2] - U_t[\boldsymbol{\theta}^2] P_\beta) |G[\boldsymbol{\theta}^1]\rangle. \end{aligned} \quad (\text{A4})$$

Finally, performing a Z measurement on the ancilla qubit, $\langle \Psi | \hat{\sigma}^z \otimes I^{\otimes N_q} | \Psi \rangle$, yields $I_{\alpha,\beta}^{p,q} = 2p_{|0\rangle} - 1$ as defined in Eq. (14), where $p_{|0\rangle}$ is the probability that the ancilla is measured to be in the state $|0\rangle$.

Appendix B: Lehmann representation of spectral function

In this appendix, we derive the Lehmann representation of the spectral function. Using the completeness relation $\hat{I} = \sum_\nu |\Psi_\nu\rangle \langle \Psi_\nu|$, where $|\Psi_\nu\rangle$ are the eigenstates of the Fermionic Hamiltonian $\hat{\mathcal{H}}$ with energies E_ν , Eq. (9) can be written as

$$\begin{aligned} G_{p,q}^R(t) &= -i\Theta(t) \left[e^{i(E_0 - E_\nu)t} M_{0,\nu}^p (M_{0,\nu}^q)^* \right. \\ &\quad \left. e^{i(E_0 - E_\nu)t} M_{\nu,0}^p (M_{\nu,0}^q)^* \right], \end{aligned} \quad (\text{B1})$$

with transition matrix elements $M_{\mu,\nu}^p \equiv \langle \Psi_\mu | \hat{c}_p | \Psi_\nu \rangle$. By applying the Fourier transform

$$G_{p,q}^R(\omega) = \int_{-\infty}^{\infty} dt e^{i(\omega + i\varepsilon)t} G_{p,q}^R(t) \quad (\text{B2})$$

with an infinitesimal ε to guarantee convergence of the integral, we find

$$G_{p,q}^R(\omega) = \sum_\nu \left[\frac{M_{0,\nu}^p (M_{0,\nu}^q)^*}{E_0 - E_\nu + \omega + i\varepsilon} + \frac{M_{\nu,0}^p (M_{\nu,0}^q)^*}{E_\nu - E_0 + \omega + i\varepsilon} \right]. \quad (\text{B3})$$

Finally, the retarded Green's function in momentum space is given by

$$\begin{aligned} G_k^R &= \frac{1}{N} \sum_{p,q} G_{p,q}^R e^{-ik(p-q)} \\ &= \frac{1}{N} \sum_{p,q} \sum_\nu \left[\frac{M_{0,\nu}^p (M_{0,\nu}^q)^*}{E_0 - E_\nu + \omega + i\varepsilon} \right. \\ &\quad \left. + \frac{M_{\nu,0}^p (M_{\nu,0}^q)^*}{E_\nu - E_0 + \omega + i\varepsilon} \right] e^{-ik(p-q)}, \end{aligned} \quad (\text{B4})$$

which simplifies to Eq. (22) for $k = 0$.

Appendix C: Quantum circuit for calculating the third-order susceptibility

In this appendix, we demonstrate that the quantum circuit presented in Fig. 4 (b) yields the imaginary part of the expectation value $\langle G[\boldsymbol{\theta}^1] | P_0 P_1 U_\tau^\dagger[\boldsymbol{\theta}^3] U_t^\dagger[\boldsymbol{\theta}^2] P_2 U_t[\boldsymbol{\theta}^2] P_3 U_\tau[\boldsymbol{\theta}^3] P_4 P_5 | G[\boldsymbol{\theta}^1] \rangle$. The system is initialized in a reference product state $|\varphi_0\rangle$. The ground state is prepared by applying the unitary operator $U_G[\boldsymbol{\theta}^1]$ using AVQITE, leading to $|G[\boldsymbol{\theta}^1]\rangle = U_G[\boldsymbol{\theta}^1]|\varphi_0\rangle$. The ancilla qubit, initially in the state $|0\rangle$, is given by $2^{-1/2}(|0\rangle + i|1\rangle)$ after applying the Hadamard gate H and phase gate $P(\varphi)$ with phase $\varphi = \pi/2$. As a result, the quantum state before applying the controlled P_5 gate reads

$$|\Psi\rangle = \frac{1}{\sqrt{2}} [|0\rangle \otimes |G[\boldsymbol{\theta}^1]\rangle + i |1\rangle \otimes |G[\boldsymbol{\theta}^1]\rangle]. \quad (\text{C1})$$

Applying the controlled P_5 and P_4 operations controlled by the ancilla qubit leads to the quantum state

$$|\Psi\rangle = \frac{1}{\sqrt{2}} [|0\rangle \otimes |G[\boldsymbol{\theta}^1]\rangle + i |1\rangle \otimes P_4 P_5 |G[\boldsymbol{\theta}^1]\rangle]. \quad (\text{C2})$$

Applying the X gate on the ancilla qubit followed by the controlled P_0 and P_1 gates yields

$$|\Psi\rangle = \frac{1}{\sqrt{2}} [|1\rangle \otimes P_1 P_0 |G[\boldsymbol{\theta}^1]\rangle + i |0\rangle \otimes P_4 P_5 |G[\boldsymbol{\theta}^1]\rangle]. \quad (\text{C3})$$

The time-evolving state under AVQDS with time-dependent variational parameters $\theta^1(\tau)$ and $\theta^3(\tau)$ becomes

$$|\Psi\rangle = \frac{1}{\sqrt{2}} \left[|1\rangle \otimes U_\tau[\theta^3]P_1P_0 |G[\theta^1]\rangle + i|0\rangle \otimes U_\tau[\theta^3]P_4P_5 |G[\theta^1]\rangle \right]. \quad (\text{C4})$$

Application of the X gate followed by the controlled P_3 gate leads to

$$|\Psi\rangle = \frac{1}{\sqrt{2}} \left[|0\rangle \otimes U_\tau[\theta^3]P_1P_0 |G[\theta^1]\rangle + i|1\rangle \otimes P_3U_\tau[\theta^3]P_4P_5 |G[\theta^1]\rangle \right]. \quad (\text{C5})$$

Propagating this state in time using AVQDS with time-dependent variational parameters $\theta^1(t)$, $\theta^3(t)$, and $\theta^2(t)$ produces

$$|\Psi\rangle = \frac{1}{\sqrt{2}} \left[|0\rangle \otimes U_t[\theta^2]U_\tau[\theta^3]P_1P_0 |G[\theta^1]\rangle + i|1\rangle \otimes U_t[\theta^2]P_3U_\tau[\theta^3]P_4P_5 |G[\theta^1]\rangle \right]. \quad (\text{C6})$$

The application of the X gate followed by the controlled P_2 gate results in the state

$$|\Psi\rangle = \frac{1}{\sqrt{2}} \left[|1\rangle \otimes P_2U_t[\theta^2]U_\tau[\theta^3]P_1P_0 |G[\theta^1]\rangle + i|0\rangle \otimes U_t[\theta^2]P_3U_\tau[\theta^3]P_4P_5 |G[\theta^1]\rangle \right]. \quad (\text{C7})$$

After executing the Hadamard gate on the ancilla qubit, the quantum state is given by

$$|\Psi\rangle = \frac{1}{2} |0\rangle \otimes [P_2U_t[\theta^2]U_\tau[\theta^3]P_1P_0 + iU_t[\theta^2]P_3U_\tau[\theta^3]P_4P_5] |G[\theta^1]\rangle - \frac{1}{2} |1\rangle \otimes [P_2U_t[\theta^2]U_\tau[\theta^3]P_1P_0 - iU_t[\theta^2]P_3U_\tau[\theta^3]P_4P_5] |G[\theta^1]\rangle. \quad (\text{C8})$$

Performing a Z measurement on the ancilla qubit yields

$$\text{Im}[\langle G[\theta^1] | P_0P_1U_\tau^\dagger[\theta^3]U_t^\dagger[\theta^2]P_2U_t[\theta^2]P_3U_\tau[\theta^3]P_4P_5 |G[\theta^1]\rangle] = 2p_{|1\rangle} - 1, \quad (\text{C9})$$

where $p_{|1\rangle}$ is the probability for the ancilla to be measured in state $|1\rangle$.

Appendix D: Exact dynamics and spectrum of third-order susceptibility

In this appendix, we derive analytical expressions for the third-order susceptibility in time and frequency domains. A more detailed discussion about the linear, second, and third-order susceptibilities of the quantum spin model (34) can be found in Ref. [62].

By applying the completeness relation $\hat{I} = \sum_\nu |\Psi_\nu\rangle \langle \Psi_\nu|$ with eigenstates $|\Psi_\nu\rangle$ of the quantum spin

Hamiltonian $\hat{\mathcal{H}}$, Eq. (29) for $\alpha = \beta = \gamma = \delta = z$ can be written as

$$\chi_{zzzz}^{(3)}(t, \tau, 0) = \frac{2}{N} \Theta(t)\Theta(\tau) \sum_{\mu\nu\lambda} M_{0,\mu}^z M_{\mu,\nu}^z M_{\nu,\lambda}^z M_{\lambda,0}^z \times \text{Im} \left[e^{iE_0(t+\tau) - iE_\mu t - iE_\nu \tau} + e^{iE_\nu(t+\tau) - iE_\lambda t - iE_0 \tau} - 2e^{iE_\mu(t+\tau) - iE_\nu t - iE_\lambda \tau} \right]. \quad (\text{D1})$$

Here, E_ν denotes the eigenenergies of $\hat{\mathcal{H}}$ and $M_{j,k}^z \equiv \langle \Psi_j | \hat{S}^z | \Psi_k \rangle$ corresponds to the magnetic dipole matrix elements along the z -direction. Figure 6 (b) shows Eq. (D1) calculated for the two-site spin-1 model. The eigenenergies and eigenstates E_μ and Ψ_ν used to calculate $\chi_{zzzz}^{(3)}(t, \tau, 0)$ were obtained using exact diagonalization.

To transform $\chi_{zzzz}^{(3)}(t, \tau, 0)$ to the 2D frequency space, the 2D Fourier transform

$$\chi_{zzzz}^{(3)}(\omega_t, \omega_\tau, 0) = \int_0^\infty dt \int_0^\infty d\tau \chi_{zzzz}^{(3)}(t, \tau, 0) e^{i(\omega_t + i0^+)t} e^{i(\omega_\tau + i0^+)\tau} \quad (\text{D2})$$

is applied, yielding [62]

$$\chi_{zzzz}^{(3)}(\omega_t, \omega_\tau, 0) = \frac{i}{N} \sum_{\mu,\nu,\lambda} S_{zzzz}^{\mu,\nu,\lambda} [L_{0,\mu}(\omega_t)L_{0,\nu}(\omega_\tau) - L_{\mu,\nu}(\omega_t)L_{0,\nu}(\omega_\tau) - 2L_{\mu,\nu}(\omega_t)L_{\mu,\lambda}(\omega_\tau) + 2L_{\nu,\lambda}(\omega_t)L_{\mu,\lambda}(\omega_\tau) + L_{\nu,\lambda}(\omega_t)L_{\nu,0}(\omega_\tau) - L_{\lambda,0}(\omega_t)L_{\nu,0}(\omega_\tau)], \quad (\text{D3})$$

where

$$S_{zzzz}^{\mu,\nu,\lambda} \equiv M_{0,\mu}^z M_{\mu,\nu}^z M_{\nu,\lambda}^z M_{\lambda,0}^z, \quad (\text{D4})$$

and

$$L_{\mu,\nu}(\omega) = \frac{1}{\omega + i0^+ + E_\mu - E_\nu} \quad (\text{D5})$$

with 0^+ denoting an infinitesimal positive quantity. According to Eq. (D3), the peaks in the 2D spectra of the third-order susceptibility in Figs. 6 (e) and 6 (f) emerge at energies determined by differences between eigenenergies $E_\mu - E_\nu$ along both the ω_t - and ω_τ -axes. Consequently, these energy positions along ω_t and ω_τ in $\chi_{zzzz}^{(3)}(\omega_t, \omega_\tau, 0)$ describe two transitions between distinct eigenstates. The magnitude of the peaks in the 2D spectra is governed by $S_{zzzz}^{\mu,\nu,\lambda}$, along with the count of contributing transitions to the signals.

Appendix E: Spectral function calculated with Padé approximation vs. discrete Fourier transformation

In this appendix, we demonstrate that the Padé approximation accelerates the convergence of the Fourier

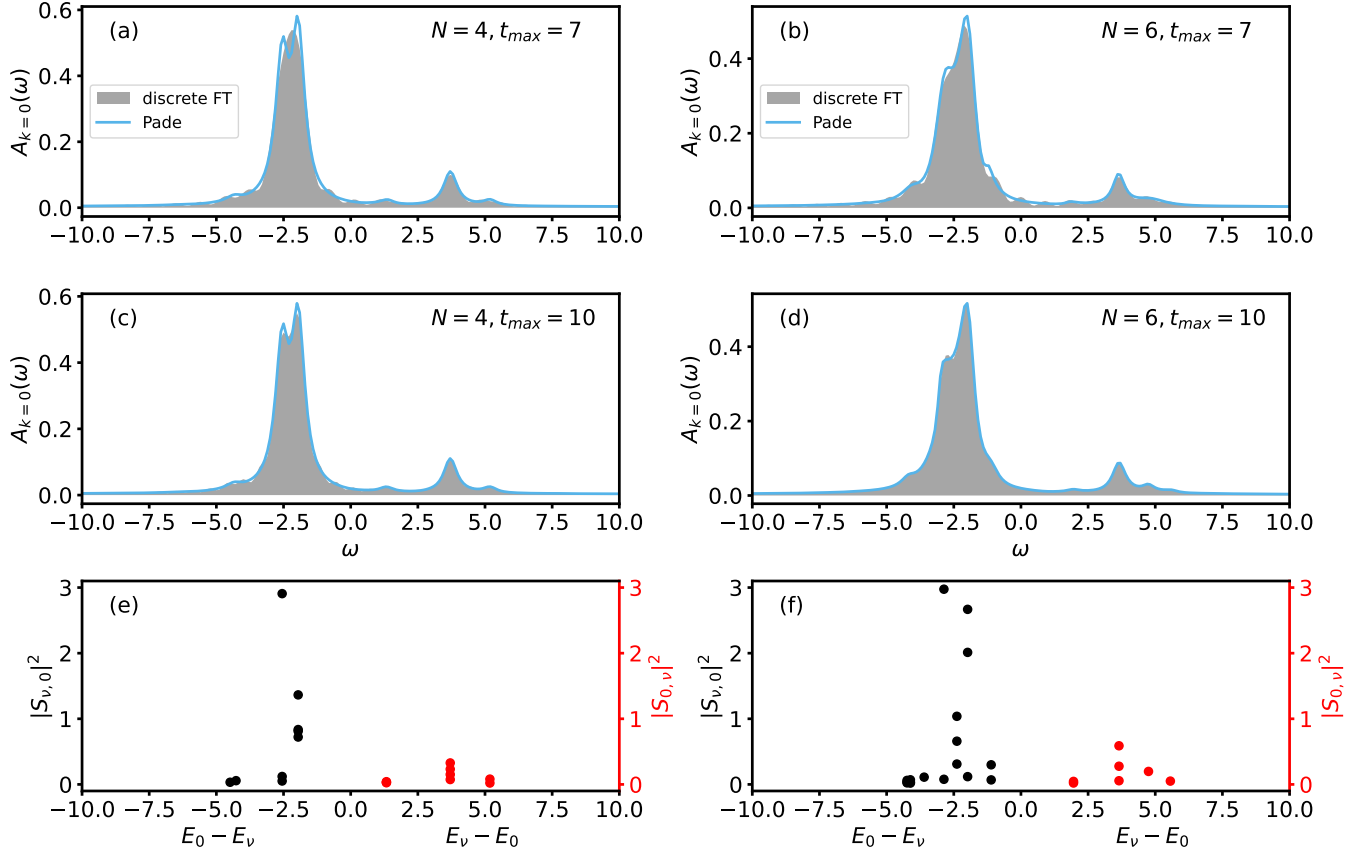


FIG. 7. **Spectral functions calculated with Padé approximation vs. discrete Fourier transformation.** (a), (b) Spectral function $A_{k=0}(\omega)$ obtained by Fourier transforming the Green's function dynamics presented in Fig. 3 (a) for $N = 4$ and 3 (b) for $N = 6$ and calculating Eq. (18). The spectral function obtained by using the discrete Fourier transformation (20) (shaded area) is shown alongside the one calculated using the Padé approximation (blue line). These results are obtained for a maximum simulation time of $t_{\max} = 7$ and a damping factor of $\varepsilon = 0.5$ in the Fourier transformation. (c), (d) The corresponding results for $t_{\max} = 10$. Compared to the spectral function obtained with Padé approximation, $A_{k=0}(\omega)$ calculated with discrete Fourier transformation requires a larger maximum simulation time to achieve comparable accuracy. (e), (f) $|S_{\nu,0}|^2$ (black dots) and $|S_{0,\nu}|^2$ (red dots) as a function of the energy differences $E_0 - E_\nu$ and $E_\nu - E_0$, respectively, for (e) $N = 4$ and (f) $N = 6$. Only the dominant transition amplitudes with $|S_{\nu,\mu}|^2 > 0.02$ are shown. The peaks in the spectral functions result from transitions between the ground state with energy E_0 to the excited states with energies E_ν , and vice versa.

transform with respect to the required maximum simulation time compared to discrete Fourier transformation. Figures 7 (a) and 7 (b) present the spectral function $A_{k=0}(\omega)$ obtained by calculating the Fourier transform of the real-time Green's function shown in Figs. 3 (a) for $N = 4$ and 3 (b) for $N = 6$, and evaluating Eq. (18). The spectral function obtained using the discrete Fourier transformation (20) (shaded area) is compared with the one calculated using the Padé approximation (blue line). These results are obtained for a maximum simulation time of $t_{\max} = 7$ and a damping factor of $\varepsilon = 0.5$ in the Fourier transformation. The corresponding results for $t_{\max} = 10$ are shown in Figs. 7 (c) and 7 (d). The spectral function obtained with the Padé approximation using $t_{\max} = 7$ resolves the dominant transitions between the ground state with energy E_0 to the excited states with energies E_ν , and vice versa. This is seen by comparing

the spectral functions in Figs. 7 (a) and 7 (b) with the corresponding transition amplitudes $|S_{\nu,0}|^2$ (black dots) and $|S_{0,\nu}|^2$ (red dots) plotted in Figs. 7 (e) and 7 (f). In contrast, the spectral function obtained with discrete Fourier transformation using $t_{\max} = 7$ does not resolve all dominant transitions in Figs. 7 (e) and 7 (f). For example, the splitting of the main peak in Fig. 7 (a) is not resolved in the spectral function calculated with the discrete Fourier transformation (shaded area). This demonstrates that the accurate calculation of the spectral function with the discrete Fourier transformation requires a larger t_{\max} . Specifically, for a maximum simulation time of $t_{\max} = 10$ (Figs. 7 (c) and 7 (d)), the spectral functions obtained with the discrete Fourier transformation show comparable accuracy to those calculated with the Padé approximation.

-
- [1] H. Bruus and K. Flensberg, *Many-Body Quantum Theory in Condensed Matter Physics: An Introduction*, Oxford Graduate Texts (OUP Oxford, 2004).
- [2] G. Stefanucci and R. van Leeuwen, *Nonequilibrium Many-Body Theory of Quantum Systems: A Modern Introduction* (Cambridge University Press, 2013).
- [3] S. Mukamel, *Principles of Nonlinear Optical Spectroscopy*, Oxford series in optical and imaging sciences (Oxford University Press, 1995).
- [4] Y. Wan and N. P. Armitage, Phys. Rev. Lett. **122**, 257401 (2019).
- [5] R. M. Nandkishore, W. Choi, and Y. B. Kim, Phys. Rev. Res. **3**, 013254 (2021).
- [6] F. Aryasetiawan and O. Gunnarsson, Reports on Progress in Physics **61**, 237 (1998).
- [7] A. Georges, G. Kotliar, W. Krauth, and M. J. Rozenberg, Rev. Mod. Phys. **68**, 13 (1996).
- [8] G. Kotliar, S. Y. Savrasov, K. Haule, V. S. Oudovenko, O. Parcollet, and C. Marianetti, Rev. Mod. Phys. **78**, 865 (2006).
- [9] H. Aoki, N. Tsuji, M. Eckstein, M. Kollar, T. Oka, and P. Werner, Rev. Mod. Phys. **86**, 779 (2014).
- [10] N. Kopnin, *Theory of Nonequilibrium Superconductivity*, International Series of Monographs on Physics (Clarendon Press, 2001).
- [11] U. Schollwöck, J. Richter, D. Farnell, and R. Bishop, *Quantum Magnetism*, Lecture Notes in Physics (Springer Berlin Heidelberg, 2008).
- [12] V. Gurarie, Phys. Rev. B **83**, 085426 (2011).
- [13] A. Damascelli, Physica Scripta **2004**, 61 (2004).
- [14] G. Mahan, *Many-Particle Physics*, Physics of Solids and Liquids (Springer US, 2012).
- [15] S. Lovesey, *Theory of Neutron Scattering from Condensed Matter*, International series of monographs on physics (Clarendon Press, 1986).
- [16] W. Kuehn, K. Reimann, M. Woerner, and T. Elsaesser, J. Chem. Phys. **130**, 164503 (2009).
- [17] W. Kuehn, K. Reimann, M. Woerner, T. Elsaesser, and R. Hey, J. Phys. Chem. B **115**, 5448 (2011).
- [18] F. Junginger, B. Mayer, C. Schmidt, O. Schubert, S. Mährlein, A. Leitenstorfer, R. Huber, and A. Pashkin, Phys. Rev. Lett. **109**, 147403 (2012).
- [19] M. Woerner, W. Kuehn, P. Bownan, K. Reimann, and T. Elsaesser, New J. Phys. **15**, 025039 (2013).
- [20] T. Maag, A. Bayer, S. Baierl, M. Hohenleutner, T. Korn, C. Schüller, D. Schuh, D. Bougeard, C. Lange, R. Huber, M. Mootz, J. E. Sipe, S. W. Koch, and M. Kira, Nat. Phys. **12**, 119 (2016).
- [21] X. Yang, C. Vaswani, C. Sundahl, M. Mootz, P. Gagel, L. Luo, J. Kang, P. Orth, I. Perakis, C. Eom, *et al.*, Nat. Mater. **17**, 586 (2018).
- [22] C. L. Johnson, B. E. Knighton, and J. A. Johnson, Phys. Rev. Lett. **122**, 073901 (2019).
- [23] L. Luo, M. Mootz, J. H. Kang, C. Huang, K. Eom, J. W. Lee, C. Vaswani, Y. G. Collantes, E. E. Hellstrom, I. E. Perakis, C. B. Eom, and J. Wang, Nat. Phys. **19**, 201 (2023).
- [24] L. Luo, X. Yang, X. Liu, Z. Liu, C. Vaswani, D. Cheng, M. Mootz, X. Zhao, Y. Yao, C.-Z. Wang, K.-M. Ho, I. E. Perakis, M. Dobrowolska, J. K. Furdyna, and J. Wang, Nat. Commun. **10**, 607 (2019).
- [25] X. Yang, C. Vaswani, C. Sundahl, M. Mootz, L. Luo, J. H. Kang, I. E. Perakis, C. B. Eom, and J. Wang, Nat. Photon. **13**, 707 (2019).
- [26] C. Vaswani, M. Mootz, C. Sundahl, D. H. Mudiyansele, J. H. Kang, X. Yang, D. Cheng, C. Huang, R. H. J. Kim, Z. Liu, L. Luo, I. E. Perakis, C. B. Eom, and J. Wang, Phys. Rev. Lett. **124**, 207003 (2020).
- [27] C. Vaswani, L.-L. Wang, D. H. Mudiyansele, Q. Li, P. M. Lozano, G. D. Gu, D. Cheng, B. Song, L. Luo, R. H. J. Kim, C. Huang, Z. Liu, M. Mootz, I. E. Perakis, Y. Yao, K. M. Ho, and J. Wang, Phys. Rev. X **10**, 021013 (2020).
- [28] X. Yang, L. Luo, C. Vaswani, X. Zhao, Y.-X. Yao, D. Cheng, Z. Liu, R. H. Kim, X. Liu, M. Dobrowolska-Furdyna, *et al.*, npj Quantum Mater. **5**, 13 (2020).
- [29] F. Mahmood, D. Chaudhuri, S. Gopalakrishnan, R. Nandkishore, and N. P. Armitage, Nat. Phys. **17**, 627 (2021).
- [30] C. Vaswani, J. H. Kang, M. Mootz, L. Luo, X. Yang, C. Sundahl, D. Cheng, C. Huang, R. H. J. Kim, Z. Liu, Y. G. Collantes, E. E. Hellstrom, I. E. Perakis, C. B. Eom, and J. Wang, Nat. Commun. **12**, 258 (2021).
- [31] B. Song, X. Yang, C. Sundahl, J.-H. Kang, M. Mootz, Y. Yao, I. Perakis, L. Luo, C. Eom, and J. Wang, Ultrafast Sci. **3**, 0007 (2023).
- [32] S. Isakov and M. Danilov, Comput. Phys. Commun. **225**, 128 (2018).
- [33] U. Schollwoeck, Ann. Phys. **326**, 96 (2011).
- [34] J. Gubernatis, N. Kawashima, and P. Werner, *Quantum Monte Carlo Methods: Algorithms for Lattice Models* (Cambridge University Press, 2016).
- [35] R. P. Feynman, Int. J. Theor. Phys. **21**, 467 (1982).
- [36] A. J. Daley, I. Bloch, C. Kokail, S. Flannigan, N. Pearson, M. Troyer, and P. Zoller, Nature **607**, 667 (2022).
- [37] J. Preskill, Quantum **2**, 79 (2018).
- [38] C. Hempel, C. Maier, J. Romero, J. McClean, T. Monz, H. Shen, P. Jurcevic, B. P. Lanyon, P. Love, R. Babbush, A. Aspuru-Guzik, R. Blatt, and C. F. Roos, Phys. Rev. X **8**, 031022 (2018).
- [39] A. Kandala, A. Mezzacapo, K. Temme, M. Takita, M. Brink, J. M. Chow, and J. M. Gambetta, Nature **549**, 242 (2017).
- [40] A. Francis, J. K. Freericks, and A. F. Kemper, Phys. Rev. B **101**, 014411 (2020).
- [41] I.-C. Chen, B. Burdick, Y.-X. Yao, P. P. Orth, and T. Iadecola, Phys. Rev. Res. **4**, 043027 (2022).
- [42] J. S. Pedernales, R. Di Candia, I. L. Egusquiza, J. Casanova, and E. Solano, Phys. Rev. Lett. **113**, 020505 (2014).
- [43] T. E. Baker, Phys. Rev. A **103**, 032404 (2021).
- [44] D. Wecker, M. B. Hastings, N. Wiebe, B. K. Clark, C. Nayak, and M. Troyer, Phys. Rev. A **92**, 062318 (2015).
- [45] T. Kosugi and Y.-i. Matsushita, Phys. Rev. A **101**, 012330 (2020).
- [46] A. Roggero and J. Carlson, Phys. Rev. C **100**, 034610 (2019).
- [47] B. Bauer, D. Wecker, A. J. Millis, M. B. Hastings, and M. Troyer, Phys. Rev. X **6**, 031045 (2016).
- [48] J. M. Kreula, S. R. Clark, and D. Jaksch, Scientific Reports **6**, 32940 (2016).

- [49] A. Chiesa, F. Tacchino, M. Grossi, P. Santini, I. Tavernelli, D. Gerace, and S. Carretta, *Nature Physics* **15**, 455 (2019).
- [50] S. Endo, I. Kurata, and Y. O. Nakagawa, *Phys. Rev. Res.* **2**, 033281 (2020).
- [51] H. Chen, M. Nusspickel, J. Tilly, and G. H. Booth, *Phys. Rev. A* **104**, 032405 (2021).
- [52] T. Keen, B. Peng, K. Kowalski, P. Lougovski, and S. Johnston, *Quantum* **6**, 675 (2022).
- [53] T. Steckmann, T. Keen, E. Kökcü, A. F. Kemper, E. F. Dumitrescu, and Y. Wang, *Phys. Rev. Res.* **5**, 023198 (2023).
- [54] X. Yuan, S. Endo, Q. Zhao, Y. Li, and S. C. Benjamin, *Quantum* **3**, 191 (2019).
- [55] F. Libbi, J. Rizzo, F. Tacchino, N. Marzari, and I. Tavernelli, *Phys. Rev. Res.* **4**, 043038 (2022).
- [56] S. Endo, J. Sun, Y. Li, S. C. Benjamin, and X. Yuan, *Phys. Rev. Lett.* **125**, 010501 (2020).
- [57] L. Nagano, A. Bapat, and C. W. Bauer, “Quench dynamics of the schwinger model via variational quantum algorithms,” (2023), arXiv:2302.10933 [hep-ph].
- [58] Y.-X. Yao, N. Gomes, F. Zhang, C.-Z. Wang, K.-M. Ho, T. Iadecola, and P. P. Orth, *PRX Quantum* **2**, 030307 (2021).
- [59] N. Gomes, A. Mukherjee, F. Zhang, T. Iadecola, C.-Z. Wang, K.-M. Ho, P. P. Orth, and Y.-X. Yao, *Adv. Quantum Technol.* **4**, 2100114 (2021).
- [60] H. R. Grimsley, S. E. Economou, E. Barnes, and N. J. Mayhall, *Nat. Commun.* **10**, 3007 (2019).
- [61] N. Gomes, D. B. Williams-Young, and W. A. de Jong, *Journal of Chemical Theory and Computation* **19**, 3313 (2023).
- [62] M. Mootz, P. P. Orth, C. Huang, L. Luo, J. Wang, and Y.-X. Yao, “Two-dimensional coherent spectrum of high-spin models via a quantum computing approach,” (2023), arXiv:2311.14035 [quant-ph].
- [63] A. McLachlan, *Mol. Phys.* **8**, 39 (1964).
- [64] J. J. Meyer, “Fisher information in noisy intermediate-scale quantum applications,” (2021), arXiv:2103.15191 [quant-ph].
- [65] P. Jordan and E. P. Wigner, in *The Collected Works of Eugene Paul Wigner* (Springer-Verlag Berlin Heidelberg New York, 1993) pp. 109–129.
- [66] S. Lloyd, *Science* **273**, 1073 (1996).
- [67] A. Smith, M. Kim, F. Pollmann, and J. Knolle, *npj Quantum Inf.* **5**, 1 (2019).
- [68] A. M. Childs, D. Maslov, Y. Nam, N. J. Ross, and Y. Su, *PNAS* **115**, 9456 (2018).
- [69] H. L. Tang, V. Shkolnikov, G. S. Barron, H. R. Grimsley, N. J. Mayhall, E. Barnes, and S. E. Economou, *PRX Quantum* **2**, 020310 (2021).
- [70] N. Gomes, F. Zhang, N. F. Berthussen, C.-Z. Wang, K.-M. Ho, P. P. Orth, and Y.-X. Yao, *J. Chem. Theory Comput.* **16**, 6256 (2020).
- [71] Y. S. Yordanov, V. Armaos, C. H. Barnes, and D. R. Arvidsson-Shukur, *Commun. Phys.* **4**, 1 (2021).
- [72] A. Mukherjee, N. F. Berthussen, J. C. Getelina, P. P. Orth, and Y.-X. Yao, *Commun. Phys.* **6**, 4 (2023).
- [73] I. G. Ryabinkin, T.-C. Yen, S. N. Genin, and A. F. Izmaylov, *J. Chem. Theory Comput.* **14**, 6317 (2018).
- [74] A. Bruner, D. LaMaster, and K. Lopata, *Journal of chemical theory and computation* **12**, 3741 (2016).
- [75] A. Bruner, D. LaMaster, and K. Lopata, *Journal of Chemical Theory and Computation* **12**, 3741 (2016).
- [76] P. Virtanen, R. Gommers, T. E. Oliphant, M. Haberland, T. Reddy, D. Cournapeau, E. Burovski, P. Peterson, W. Weckesser, J. Bright, *et al.*, *Nat. Methods* **17**, 261 (2020).
- [77] W. Choi, K. H. Lee, and Y. B. Kim, *Phys. Rev. Lett.* **124**, 117205 (2020).
- [78] Y. Wang, Z. Hu, B. C. Sanders, and S. Kais, *Front. Phys.* **8**, 1 (2020).
- [79] O. Ogunkoya, J. Kim, B. Peng, A. B. i. e. i. f. m. c. Özgüiler, and Y. Alexeev, *Phys. Rev. A* **109**, 012426 (2024).
- [80] R. Dutta, D. G. Cabral, N. Lyu, N. P. Vu, Y. Wang, B. Allen, X. Dan, R. G. Cortiñas, P. Khazaei, S. E. Smart, *et al.*, arXiv:2404.10214 (2024), 10.48550/arXiv.2404.10214.
- [81] T. J. Stavenger, E. Crane, K. C. Smith, C. T. Kang, S. M. Girvin, and N. Wiebe, in *2022 IEEE High Performance Extreme Computing Conference (HPEC)* (IEEE, 2022) pp. 1–8.
- [82] J. a. C. Getelina, C.-Z. Wang, T. Iadecola, Y.-X. Yao, and P. P. Orth, *Phys. Rev. B* **109**, 085128 (2024).
- [83] O. Di Matteo, A. McCoy, P. Gysbers, T. Miyagi, R. M. Woloshyn, and P. Navrátil, *Phys. Rev. A* **103**, 042405 (2021).
- [84] Z. Cai, R. Babbush, S. C. Benjamin, S. Endo, W. J. Huggins, Y. Li, J. R. McClean, and T. E. O’Brien, *Rev. Mod. Phys.* **95**, 045005 (2023).
- [85] J. C. Getelina, P. Sharma, T. Iadecola, P. P. Orth, and Y.-X. Yao, arXiv e-prints, arXiv:2404.09132 (2024), arXiv:2404.09132.